

New and updated timing models for seven young energetic X-ray pulsars, including the Big Glitcher PSR J0537–6910

Wynn C. G. Ho,¹★ Lucien Kuiper,² Cristóbal M. Espinoza,^{3,4} Timothy Leon,¹ Bennett Waybright,¹

Sebastien Guillot,^{5,6} Zaven Arzoumanian,⁷ Slavko Bogdanov,⁸ and Alice K. Harding⁹

¹Department of Physics and Astronomy, Haverford College, 370 Lancaster Avenue, Haverford, PA 19041, USA

²Space Research Organisation Netherlands, Niels Bohrweg 4, 2333 CA, Leiden, Netherlands

³Departamento de Física, Universidad de Santiago de Chile (USACH), Av. Víctor Jara 3493, Estación Central, Chile

⁴Center for Interdisciplinary Research in Astrophysics and Space Sciences (CIRAS), Universidad de Santiago de Chile, Santiago, Chile

⁵IRAP, CNRS, 9 avenue du Colonel Roche, BP 44346, 31028 Toulouse Cedex 4, France

⁶Université de Toulouse, CNES, UPS-OMP, 31028 Toulouse, France

⁷X-Ray Astrophysics Laboratory, NASA Goddard Space Flight Center, Greenbelt, MD, 20771, USA

⁸Columbia Astrophysics Laboratory, Columbia University, 550 West 120th Street, New York, NY 10027, USA

⁹Theoretical Division, Los Alamos National Laboratory, Los Alamos, NM 87545, USA

Accepted 2025 December 19. Received 2025 December 4; in original form 2025 October 28

ABSTRACT

We present new timing models and update our previous ones for the rotational evolution of seven young energetic pulsars, including four of the top five in spin-down luminosity \dot{E} among all known pulsars. For each of the six pulsars that were monitored on a regular basis by NICER, their rotation phase-connected timing model covers the entire period of NICER observations, in many cases from 2017–2025. For PSR J0058–7218, which was only identified in 2021, we extend the baseline of its timing model by 3 years and report detections of its first three glitches. The timing model for PSR J0537–6910 over the entire 8 years of NICER monitoring is presented, including a total of 23 glitches; we also report its spin frequency and pulsed spectrum from a 2016 NuSTAR observation. For PSR B0540–69, its complete timing model from 2015–2025 is provided, including a braking index evolution from near 0 to 1.6 during this period. The 8-year timing model for PSR J1412+7922 (also known as Calvera) is reported, which includes a position that is consistent with that measured from imaging. For PSR J1811–1925, we present its 3.5-year timing model. For PSR J1813–1749, its incoherent timing model is extended through early 2025 using new Chandra observations. For PSR J1849–0001, its 7-year timing model is provided, including a position that is consistent with and more accurate than its imaging position and its first glitch that is one of the largest ever measured. Our timing models of these seven X-ray pulsars enable their study at other energies and in gravitational wave data.

Key words: pulsars: general – pulsars: individual: PSR J0058–7218, PSR J0537–6910, PSR B0540–69, PSR J1412+7922, PSR J1811–1925, PSR J1813–1749, PSR J1849–0001 – stars: neutron – X-rays: stars

1 INTRODUCTION

Long-term monitoring and timing observations to measure the rotational evolution of pulsars are crucial for studying their individual properties, for classifying them, and for using them to study fundamental physics and gravity. For example, sudden measured changes in the spin frequency, also known as glitches, of some pulsars provide crucial insights into neutron star crust properties and superfluidity in dense nuclear matter (see, e.g., Antonopoulou et al. 2022, for review). Precision timing of millisecond pulsars allowed detection of low frequency gravitational waves produced by binary inspirals of supermassive black holes (Agazie et al. 2023). Pulsar timing also enables the most sensitive searches for high frequency

gravitational waves produced by isolated and binary pulsars (e.g., Abac et al. 2025).

Here we present updates of the timing models, or ephemerides, of six young energetic pulsars that were reported in Ho et al. (2022) and Espinoza et al. (2024), as well as the timing model of one other young energetic pulsar, PSR J1811–1925. For six of the seven timing models, the models are rotation phase-connected and are therefore tracking each individual rotation of the pulsar. The seven pulsars are predominantly only observable in the X-ray, and the data used here are primarily from regular monitoring observations made by the Neutron Star Interior Composition Explorer (NICER; Gendreau et al. 2016) during its entire lifetime from 2017 to 2025. Some of the properties of these seven pulsars are given in Table 1, and their location within the P – \dot{P} diagram of pulsars is shown in Figure 1, where P and \dot{P} are the pulsar spin period and spin period time derivative, respectively, and the relation of the former to pulsar spin frequency is $\nu = 1/P$.

★ E-mail: who@haverford.edu

Table 1. Properties of pulsars considered in present work. Spin period P and spin period time derivative \dot{P} , spin-down luminosity $\dot{E} = 4.0 \times 10^{46} \text{ erg s}^{-1} \dot{P}/P^3$, magnetic field $B = 3.2 \times 10^{19} \text{ G} (P\dot{P})^{1/2}$, characteristic age $\tau_c \equiv P/2\dot{P}$, supernova remnant (SNR) association and age, and distance d . References: [1] Owen et al. (2011), [2] Graczyk et al. (2020), [3] Chen et al. (2006), [4] Pietrzyński et al. (2019), [5] Arias et al. (2022), [6] Greco et al. (2025), [7] Mereghetti et al. (2021), [8] Borkowski et al. (2016), [9] Kilpatrick et al. (2016), [10] Brogan et al. (2005), [11] Dzib & Rodríguez (2021), [12] Camilo et al. (2021), [13] Gotthelf et al. (2011).

Pulsar	P (ms)	\dot{P} ($10^{-14} \text{ s s}^{-1}$)	\dot{E} ($10^{37} \text{ erg s}^{-1}$)	B (10^{12} G)	τ_c (kyr)	SNR	SNR age (kyr)	d (kpc)
PSR J0058–7218	21.8	2.95	11	0.81	11.7	IKT 16	14.7 [1]	62 [2]
PSR J0537–6910	16.2	5.21	49	0.93	4.91	N157B	1–5 [3]	49.6 [4]
PSR B0540–69	50.7	47.9	15	5.0	1.68	0540–69.3		49.6 [4]
PSR J1412+7922	59.2	0.330	0.064	0.45	285	G118.4+37.0	10–20 [5,6]	3–5 [6,7]
PSR J1811–1925	64.7	4.40	0.65	1.7	24	G11.2–0.3	1.4–2.4 [8]	7.2 [9]
PSR J1813–1749	44.7	12.7	5.7	2.4	5.58	G12.82–0.02	1–2.2 [10,11]	6–14 [12]
PSR J1849–0001	38.5	1.42	0.99	0.75	43.1			7 [13]

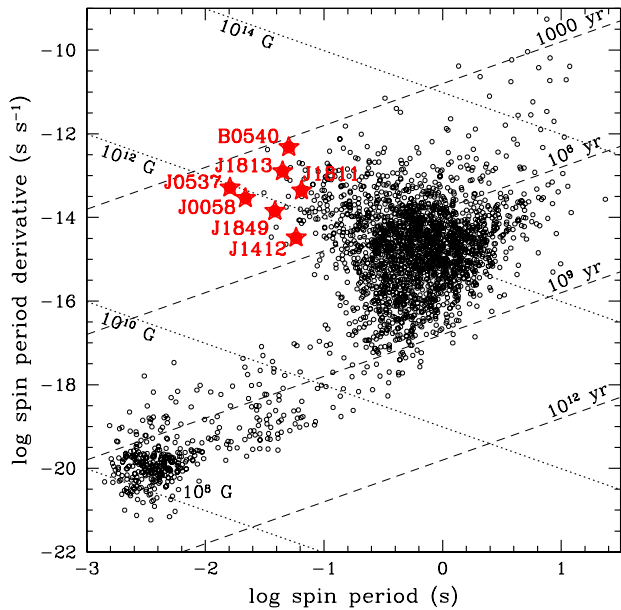


Figure 1. Pulsar spin period P and spin period time derivative \dot{P} . Circles denote pulsars whose values are taken from the ATNF Pulsar Catalogue (Manchester et al. 2005, version 2.3.0), and stars indicate pulsars considered in this work (see Table 1). Dashed lines indicate characteristic age $\tau_c \equiv P/2\dot{P}$, and dotted lines indicate magnetic field strength $B = 3.2 \times 10^{19} \text{ G} (P\dot{P})^{1/2}$.

An outline of the paper is as follows. A brief summary of each pulsar is given next in Section 1.1. Section 2 describes the Chandra, NICER, and NuSTAR data analyzed in this work and their processing. Section 3 presents our results for each of the seven pulsars, including their timing models. Section 4 summarizes the work presented here.

1.1 Summary of pulsars

PSR J0058–7218 is a relatively newly identified fast spinning young pulsar in a supernova remnant and pulsar wind nebula in the Small Magellanic Cloud (Owen et al. 2011; Maitra et al. 2015). Its timing properties were first measured by Maitra et al. (2021), and a rotation phase-connected timing model over an 8-month period was presented in Ho et al. (2022). The pulsar has a narrow single peak pulse profile and high pulsed fraction of ≈ 70 percent in the 0.4–10 keV band. Its

rapid spin-down rate means PSR J0058–7218 has the fourth highest measured spin-down luminosity \dot{E} among the ~ 3000 known pulsars.

PSR J0537–6910 (also known as Big Glitcher) is the fastest spinning young pulsar, is in the supernova remnant N157B in the Large Magellanic Cloud (Wang & Gotthelf 1998; Chen et al. 2006), and has the the highest \dot{E} among all known pulsars. PSR J0537–6910 has a narrow single peak pulse profile and X-ray pulsed fraction of ~ 20 percent (Marshall et al. 1998; Kuiper & Hermsen 2015; Ho et al. 2020b). While its spin frequency decreases (by more than 0.16 Hz since 1999) over the more than 20 years of combined observations (1999–2011 with RXTE and 2017–2025 with NICER), a remarkable 68 glitches are measured, including 23 by NICER. This yields the highest known average glitch rate of $\sim 3.4 \text{ yr}^{-1}$ (Marshall et al. 2004; Middleditch et al. 2006; Antonopoulou et al. 2018; Ferdman et al. 2018; Ho et al. 2020b, 2022; Abbott et al. 2021a). Its glitches are unusual in their predictability, in particular there is a correlation between the size of its glitches $\Delta\nu$ and time to its next glitch (Middleditch et al. 2006; Antonopoulou et al. 2018; Ferdman et al. 2018; Ho et al. 2020b, 2022). Its timing properties are also unusual, with a braking index $n \equiv \ddot{\nu}\nu/\dot{\nu}^2 = -1.25 \pm 0.01$ (1σ error) over the long-term (27-year duration) and a value that approaches $\lesssim 7$ over the short-term (~ 100 day) between glitches.

PSR B0540–69 is a young energetic pulsar (third highest \dot{E}) in a pulsar wind nebula and supernova remnant in the Large Magellanic Cloud. It is sometimes referred to as a twin of the Crab pulsar. Its spin pulsations are detected in radio (Manchester et al. 1993; Johnston & Romani 2003), optical/UV (Middleditch & Pennypacker 1985; Mignani et al. 2019), X-rays (Seward et al. 1984), and gamma-rays (Fermi LAT Collaboration et al. 2015). PSR B0540–69 undergoes small glitches and displays unusual spin-down behavior, including a large sudden change in $\dot{\nu}$ (Marshall et al. 2015) that led to an evolving braking index (see, Espinoza et al. 2024, and references therein).

PSR J1412+7922 (also known as Calvera) is a high Galactic latitude pulsar (Zane et al. 2011; Halpern et al. 2013) residing within a diffuse radio ring that seems to be a supernova remnant (Arias et al. 2022; Rigoselli et al. 2024; Greco et al. 2025). As a result, PSR J1412+7922 appears to be a member of the class of neutron stars known as central compact objects (CCOs; see De Luca 2017, for review). If the distance of ~ 3 kpc determined from modeling the pulsar's X-ray spectrum (Mereghetti et al. 2021) and the association between the pulsar and supernova remnant candidate are correct, then the age of the system is ~ 10 –20 kyr (Greco et al. 2025). Monitoring observations of PSR J1412+7922 during the first year of NICER in 2017–2018 yielded its phase-connected timing model

(Bogdanov et al. 2019), and subsequent works gradually extended the timing model to over six years using NICER data through 2023 November (Mereghetti et al. 2021; Ho et al. 2022; Rigoselli et al. 2024). Timing analysis by Ho et al. (2022) also yielded a pulsar position that is inconsistent with the position and proper motion measurements made by Halpern & Gotthelf (2015) using Chandra imaging data from 2007 and 2014. Instead, the timing position and 2014 imaging position imply a proper motion of $\mu_\alpha \cos \delta = +120 \pm 20$ mas yr $^{-1}$ and $\mu_\delta = -3 \pm 20$ mas yr $^{-1}$. A revised measurement of the position and proper motion by Rigoselli et al. (2024) using newer Chandra imaging data from 2024 found values that are much more consistent with the timing results of Ho et al. (2022) (see also Section 3.4), including a much more significant measurement of $\mu_\alpha \cos \delta = +78.1 \pm 2.9$ mas yr $^{-1}$ and $\mu_\delta = +8.0 \pm 3.0$ mas yr $^{-1}$.

PSR J1811–1925 is a young energetic pulsar in a pulsar wind nebula and supernova remnant (Torii et al. 1997, 1999; Kaspi et al. 2001). It has spin pulsations that are only detected in X-ray up to 135 keV and a high pulsed fraction of > 20 percent (Kuiper & Hermsen 2015; Madsen et al. 2020; Zheng et al. 2023; Takata et al. 2024).

PSR J1813–1749 is a young highly energetic pulsar that produces a pulsar wind nebula and is associated with the gamma-ray/TeV source IGR J18135–1751/HESS J1813–178. The pulsar's proper motion from the center of the young supernova remnant G12.82–0.02 implies an age of 1000–2200 yr (Dzib & Rodríguez 2021). PSR J1813–1749 has a broad single peak X-ray pulse profile and high X-ray pulsed fraction (Gotthelf & Halpern 2009; Halpern et al. 2012; Kuiper & Hermsen 2015; Ho et al. 2020a; Takata et al. 2024). Even though the pulsar has also been detected in radio, its radio pulses suffer from extremely high scattering (Camilo et al. 2021).

PSR J1849–0001 is another young energetic pulsar that produces a pulsar wind nebula and is associated with the gamma-ray/TeV source IGR J18490–0000/HESS J1849–000. The X-ray spectral properties of the pulsar and wind nebula have been studied in, e.g., Kuiper & Hermsen (2015); Gagnon et al. (2024); Kim et al. (2024); Takata et al. (2024). The pulsar has a broad single peak pulse profile and very high pulsed fraction (Kuiper & Hermsen 2015; Bogdanov et al. 2019; Kim et al. 2024; Takata et al. 2024). Phase-connected timing models have been derived using RXTE data (Gotthelf et al. 2011; Kuiper & Hermsen 2015) and Swift and NICER data (Bogdanov et al. 2019; Ho et al. 2022; Kim et al. 2024).

2 DATA ANALYSIS

2.1 Chandra data

Chandra observed PSR J0537–6910 twice in 2002 using the ACIS-S detector on August 23 and October 29 (ObsID 2783) for a total of about 48 ks. Chandra observed PSR J1813–1749 six times using the ACIS-S detector in continuous clocking (CC) mode on 2012 February 12 (ObsID 12549), 2021 February 10 (ObsID 23545), 2021 June 23 (ObsID 23546), 2024 April 3 (ObsID 28355), 2024 October 7 (ObsID 28356), and 2025 March 23 (ObsID 28357) for about 20 ks on each date (see Table 2). We reprocess these data following the standard procedure using `chandra_repro` of the Chandra Interactive Analysis of Observations (CIAO) package version 4.17 and Calibration Database (CALDB) 4.12.0 (Fruscione et al. 2006). For data on PSR J0537–6910, we use `specextract` to extract source events from a 1" radius circle centered on the pulsar position and with a background region consisting of a 3" \times 10" rectangular box

Table 2. Observation log

Telescope	Pulsar	Observation Date	Exposure (ks)
Chandra	PSR J0537–6910	2002 Aug 23	28
		2002 Oct 29	20
	PSR J1813–1749	2012 Feb 12	20
		2021 Feb 10	20
		2021 Jun 23	20
		2024 Apr 3	21
		2024 Oct 7	20
		2025 Mar 23	20
NICER	PSR J0058–7218	2021 Jun 1–2024 Dec 1	609
	PSR J0537–6910	2017 Aug 17–2025 Jun 1	2171
	PSR B0540–69	2017 Jul 25–2025 Jun 10	137
	PSR J1412+7922	2017 Sep 15–2025 Apr 23	1889
	PSR J1811–1925	2021 Sep 1–2025 May 23	317
	PSR J1849–0001	2018 Feb 13–2025 Jun 8	474
NuSTAR	PSR J0537–6910	2016 Oct 17	105

centered on the pulsar but excluding the source extraction circle (see Figure 4 of Chen et al. 2006). For data on PSR J1813–1749, we extract source events from the one-dimensional CC image along a 1.5" length centered on the pulsar position and with a background region 11" in length and about 10" from the source region; we also consider a larger 3" extraction length to collect more photons for spectral analysis (see Section 3.6), although this gives somewhat weaker pulse detections. Spectra are combined using `combine_spectra` and binned using `dmgroup` with a minimum of 25 counts per bin.

For timing analysis of PSR J1813–1749, we select only events in the 2–8 keV energy range. We transform the selected event time stamps from Terrestrial Time (TT) to Barycentric Dynamical Time (TDB) using `axbary` and the pulsar position. Acceleration searches for the spin frequency are conducted using PRESTO (Ransom et al. 2002) with a time bin of 2.85 ms. Data are folded at the candidate pulse frequency using `prepfold`, and a refined frequency is determined. Following the standard procedure¹, we compute rotation phases using `dmtcalc` and create good time intervals (GTIs) using `dmgti` for on-pulse emission, i.e. photons with a rotation phase around the peak of the pulse profile, and off-pulse emission, which are photons with a phase outside the on-pulse phase range. After correcting the exposure time, we extract phase resolved spectra using `specextract`. The off-pulse spectra can be used as the background for the on-pulse spectra, such that the final pulsed spectra are the result of on minus off-pulse emissions.

2.2 NICER data

For six of the seven pulsars considered in this work, we use and report analyses of new NICER data, which are summarized in Table 2. For PSR J0058–7218, PSR B0540–69, and PSR J1811–1925, searches for pulsations, generation of pulse time-of-arrival (TOA), and determination of timing models are performed following the procedures described in Kuiper & Hermsen (2009). For PSR J0537–6910, PSR J1412+7922, and PSR J1849–0001, their data are processed following the same procedures described in Ho et al. (2022), which we briefly summarize here. We refer the reader to Ho et al. (2022) for more details. Note that NICER experienced a light leak² that affected

¹ https://cxc.harvard.edu/ciao/threads/phase_bin

² https://heasarc.gsfc.nasa.gov/docs/nicer/analysis_threads/light-leak

data taken after 2023 May during orbit day. As a result, the cadence of observations was reduced, and fewer TOAs were obtained for pulsars such as PSR J0058–7218 and PSR J1412+7922 and especially for PSR J0537–6910 because of its high glitch activity. However, our ability to obtain overall timing models was not severely impacted.

We process and filter NICER data using `nicer12` of HEA-Soft 6.22–6.35.2 (HEASARC 2014) and NICERDAS 2018-03-01_V003–2025-06-11_V014. While NICER is sensitive to 0.25–12 keV photons, we extract only events within a particular energy range for each pulsar to optimize pulsation searches (1–7 keV for PSR J0537–6910, 0.37–1.97 keV for PSR J1412+7922, and 1.89–6 keV for PSR J1849–0001). We ignore time intervals of enhanced background affecting all detectors by constructing a light curve binned at 16 s and removing intervals strongly contaminated by background flaring when the count rate exceeds a threshold value that is different for each pulsar (10 c s^{-1} for PSR J0537–6910, 4.5 c s^{-1} for PSR J1412+7922, and 5 c s^{-1} for PSR J1849–0001). Using these filtering criteria, we obtain clean data for pulse timing analysis. We use `barycorr` to transform between TT, used for event time stamps, and TDB and to account for effects of satellite motion with respect to the barycenter. In all timing analyses performed here unless otherwise noted (in particular, Sections 3.4 and 3.7), source positions are held fixed at the values given in the corresponding tables below, along with our adopted solar system ephemeris. As with analysis of Chandra data, we use PRESTO and `prepfold` to perform a pulsation search and to determine the spin frequency of each pulsar. A template pulse profile for each pulsar is produced by fitting a set of NICER pulse profiles with a Gaussian shape; this template is then used to determine the TOA of each observation following the unbinned maximum likelihood technique described in Ray et al. (2011). Unless otherwise noted below, we use TEMPO2 (Hobbs et al. 2006) to fit TOAs with a timing model and to measure glitch parameters. In particular, a pulsar’s rotation phase ϕ is fit to a reference time t_0 based on a truncated Taylor series of the spin frequency and its time derivatives,

$$\phi(t) = \nu(t - t_0) + \frac{1}{2}\dot{\nu}(t - t_0)^2 + \frac{1}{6}\ddot{\nu}(t - t_0)^3 + \dots \quad (1)$$

Glitches are fit to a model at the glitch epoch t_g by

$$\begin{aligned} \phi_g = & \Delta\phi + \Delta\nu(t - t_g) + \frac{1}{2}\Delta\dot{\nu}(t - t_g)^2 + \frac{1}{6}\Delta\ddot{\nu}(t - t_g)^3 \\ & + \Delta\nu_d \tau_d [1 - e^{-(t - t_g)/\tau_d}], \end{aligned} \quad (2)$$

where the last term accounts for a post-glitch recovery $\Delta\nu_d$, if present, that occurs on a timescale τ_d .

2.3 NuSTAR data

NuSTAR observed PSR J0537–6910 on 2016 October 17 (ObsID 40201014002) for 105 ks. We reprocess this data using `nupipeline` and `nuproducts` of HEASoft 6.35.2 and NUSTARDAS 2025-03-11_v2.1.5 and barycenter events with clock correction 20100101v211 and the pulsar’s position. The source extraction region is a circle of $60''$ radius, and the background region is a circle of the same size and placed in a field with low counts. For timing analysis, we use `xselect` to choose only events at 3–20 keV. We use PRESTO and `prepfold` to perform pulsation searches on the merged FPMA and FPMB event list and to determine the spin frequency. To extract pulsed spectra, we first use `photonphase` in PINT (Luo et al. 2021) and the spin frequency to determine the rotation phase of each photon in the data. We then use `maketime` to determine GTIs for on-

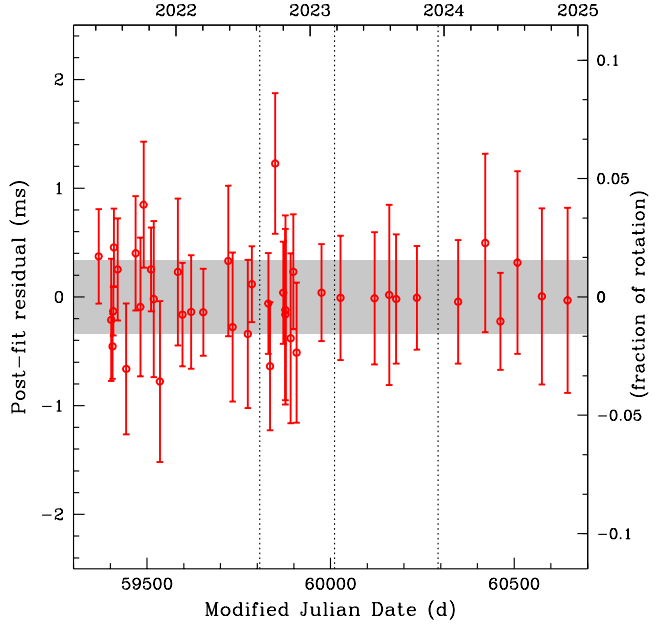


Figure 2. Timing residuals of PSR J0058–7218 from a best-fit of NICER pulse times-of-arrival with the timing model given in Table 3 and the RMS residual illustrated by the shaded region between $\pm 0.339 \text{ ms}$. Errors are 1σ uncertainty. The vertical dotted lines indicate the approximate times of 3 spin-up glitches (MJD 59807, 60011, 60293).

pulse emission and off-pulse emission. Finally, we run `nuproducts` with these GTIs to produce on and off-pulse spectra.

3 RESULTS

3.1 PSR J0058–7218

NICER observations of PSR J0058–7218 began on 2021 June 1. Ho et al. (2022) reported a phase-connected timing model through 2022 January 25. Here we extend the timing model by about 3 years with NICER data through 2024 December 1, for a total timespan of 3.5 years. Note that additional NICER data through 2025 June 1 are not of sufficient quality to enable detection of the spin pulsations of PSR J0058–7218. Figure 2 shows residuals of our best-fit timing model, which is given in Table 3.

Our regular cadence of observations of PSR J0058–7218 reveal that this young pulsar underwent three glitches during 3.5 years of monitoring. Not only does this suggest a high glitch rate for PSR J0058–7218, but two of the three glitches are large, i.e., $\Delta\nu \gtrsim 10 \mu\text{Hz}$ (see, e.g., Fuentes et al. 2017). Both these properties are typical for young pulsars, including PSR J0537–6910 and the Vela pulsar (Antonopoulou et al. 2022). Meanwhile the small glitch $\Delta\nu_1$ is accompanied by a positive change in spin-down rate, i.e., $\Delta\dot{\nu}_1 > 0$, which is contrary to typical behavior of glitches and could indicate timing noise similar to that seen in PSR B0540–69 (see Espinoza et al. 2024 and Section 3.3).

3.2 PSR J0537–6910

Because of the fast spin of PSR J0537–6910 and that its spin pulsations are only detectable in X-ray, few instruments have been able

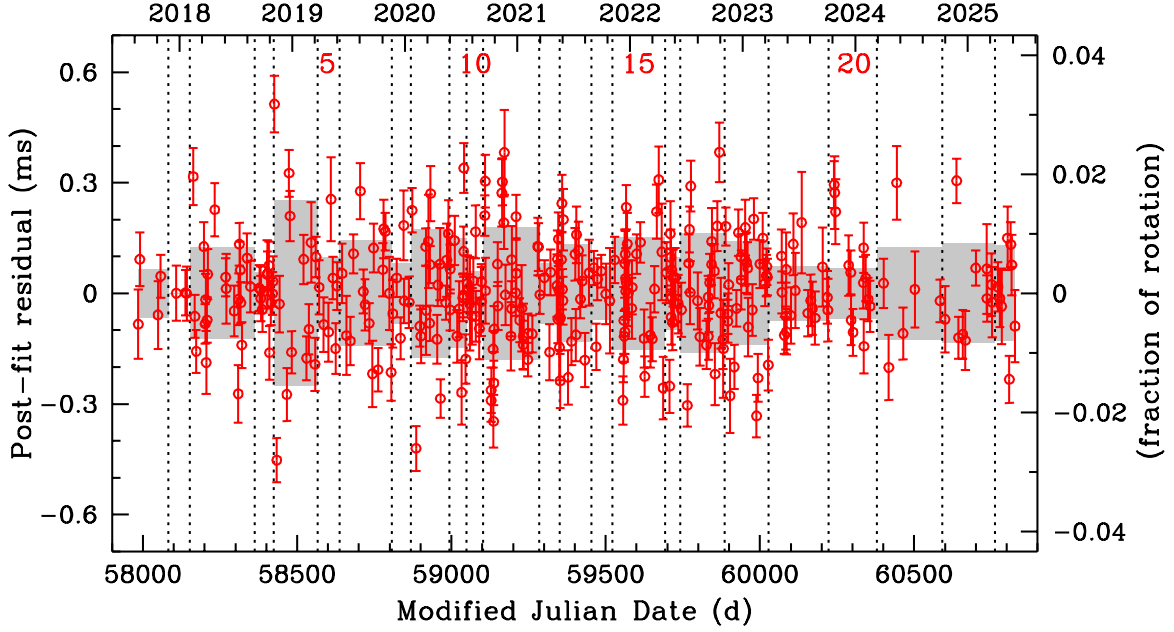


Figure 3. Timing residuals of PSR J0537–6910 from a best-fit of NICER pulse times-of-arrival with the timing model given in Table 4 and RMS residuals illustrated by the shaded regions. Errors are 1σ uncertainty. Segments are labeled by numbers and separated by the occurrence of a glitch, each of which is denoted by a vertical dotted line.

Table 3. Timing parameters of PSR J0058–7218. Numbers in parentheses are 1σ uncertainty in last digit. The position is from a Chandra ACIS-S image (MJD 56332), with a 90 percent confidence level uncertainty of $0.^{\circ}6$ (Maitra et al. 2015).

Parameter	Value
R.A. α (J2000)	$00^{\text{h}}58^{\text{m}}16.^{\text{s}}85$
Decl. δ (J2000)	$-72^{\circ}18'05.^{\text{s}}60$
Solar system ephemeris	DE405
Range of dates (MJD)	59368–60645
Epoch (MJD TDB)	59580
t_0 (MJD)	60026.9
Frequency ν (Hz)	45.93950855275(33)
Freq. 1st derivative $\dot{\nu}$ (Hz s $^{-1}$)	$-6.2263535(71) \times 10^{-11}$
Freq. 2nd derivative $\ddot{\nu}$ (Hz s $^{-2}$)	$3.962(29) \times 10^{-21}$
Glitch epoch 1 (MJD)	59807±21
$\Delta\phi_1$	0.125(28)
$\Delta\nu_1$ (Hz)	$7.35(72) \times 10^{-8}$
$\Delta\dot{\nu}_1$ (Hz s $^{-1}$)	$1.678(82) \times 10^{-14}$
Glitch epoch 2 (MJD)	60011±11
$\Delta\phi_2$	-0.029(53)
$\Delta\nu_2$ (Hz)	$3.6039(26) \times 10^{-5}$
$\Delta\dot{\nu}_2$ (Hz s $^{-1}$)	$-3.276(57) \times 10^{-13}$
$\Delta\ddot{\nu}_2$ (Hz s $^{-2}$)	$2.63(52) \times 10^{-21}$
Glitch epoch 3 (MJD)	60293±48
$\Delta\phi_3$	-0.02(16)
$\Delta\nu_3$ (Hz)	$3.1596(49) \times 10^{-5}$
$\Delta\dot{\nu}_3$ (Hz s $^{-1}$)	$-1.431(73) \times 10^{-13}$
$\Delta\ddot{\nu}_3$ (Hz s $^{-2}$)	$-1.70(57) \times 10^{-21}$
RMS residual (μ s)	338.9
χ^2/dof	18.8/28
Number of TOAs	42

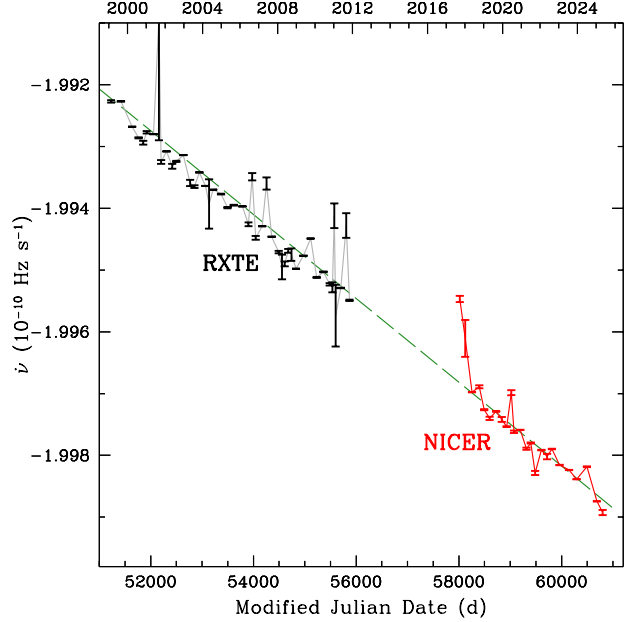


Figure 4. Evolution of spin frequency time derivative $\dot{\nu}$ of PSR J0537–6910, where $\dot{\nu}$ is from the timing model of each segment (see Table 4 for NICER and Table 1 of Antonopoulou et al. 2018 for RXTE). Errors are 1σ uncertainty. Dashed line shows a linear fit of NICER and RXTE data with best-fit $\dot{\nu} = -7.85 \times 10^{-22}$ Hz s $^{-2}$.

to track its timing properties over long periods of time. RXTE performed high-cadence observations of PSR J0537–6910 from 1999 to 2011, and these data yielded phase-connected timing models during

Table 4. Timing parameters of PSR J0537–6910. Columns are interglitch segment number, timing model epoch, segment start and end dates, spin frequency and its first two time derivatives, interglitch braking index n_{ig} ($= \ddot{\nu}\nu/\dot{\nu}^2$), timing model residual, goodness-of-fit measure, and number of times of arrival. Numbers in parentheses are 1σ uncertainty in last digit. Values for segments 1–7, 8–10, and 11–14 are similar to those given in Ho et al. (2020b), Abbott et al. (2021a), and Ho et al. (2022), respectively. Position of R.A. = $05^{\text{h}}37^{\text{m}}47^{\text{s}}.416$, decl. = $-69^{\circ}10'19''.88$ (J2000) is from a Chandra ACIS-I image (MJD 51442), with 1σ uncertainty of $\sim 0''.6$ (Townsley et al. 2006). Solar system ephemeris used is DE421.

Segment	Start (MJD)	End (MJD)	Epoch (MJD)	t_0 (MJD)	ν (Hz)	$\dot{\nu}$ (10^{-10} Hz s $^{-1}$)	$\ddot{\nu}$ (10^{-20} Hz s $^{-2}$)	n_{ig}	RMS (μs)	χ^2/dof	TOAs
0	57984	58058	58020	58049.1	61.9243742602(16)	-1.995468(50)	[1] ^a	—	66.1	3.14/1	4
1	58108	58142	58124	58138.0	61.9225972030(30)	-1.99611(30)	[1] ^a	—	1.29	— ^b	3
2	58162	58349	58255	58268.4	61.9203729962(9)	-1.9969767(20)	0.564(12)	8.75(18)	124	74.5/17	21
3	58377	58423	58399	58402.8	61.9178962511(30)	-1.996890(24)	5.95(64)	92.3(99)	56.4	8.43/7	11
4	58426	58561	58493	58482.1	61.9162995588(37)	-1.9972611(85)	0.813(82)	12.6(13)	251	183/9	13
5	58571	58630	58600	58601.6	61.9144624211(18)	-1.997402(26)	[1] ^a	—	98.5	13.1/4	7
6	58645	58805	58723	58720.0	61.9123666199(15)	-1.9972887(36)	0.880(29)	13.66(44)	143	70.8/12	16
7	58810	58863	58836	58835.0	61.9104242102(61)	-1.997420(39)	5.76(89)	89(13)	81.9	9.34/2	6
8	58872	58991	58931	58931.0	61.9088087390(25)	-1.9975354(70)	1.058(81)	16.4(13)	174	129/13	17
9	58995	59047	59020	59018.6	61.9072733762(21)	-1.996986(40)	[1] ^a	—	148	53.7/8	11
10	59050	59099	59074	59071.3	61.9063499483(47)	-1.997617(20)	3.64(81)	56(13)	60.9	8.95/6	10
11	59108	59283	59195	59195.2	61.9042953587(11)	-1.9975882(25)	0.595(17)	9.24(26)	180	229/27	31
12	59286	59350	59318	59318.2	61.9021804218(40)	-1.997892(16)	0.71(38)	11.1(60)	82.4	15.4/6	10
13	59352	59447	59399	59401.0	61.9007944153(27)	-1.9978015(93)	1.63(13)	25.3(21)	132	60/13	17
14	59461	59514	59487	59485.8	61.8992920385(27)	-1.998284(32)	[1] ^a	—	72.7	9.06/3	6
15	59529	59687	59607	59612.6	61.8972423813(11)	-1.9979145(33)	0.798(23)	12.38(36)	152	124/23	27
16	59696	59736	59716	59717.0	61.8953668356(27)	-1.998020(45)	[1] ^a	—	98.6	21.6/9	12
17	59745	59882	59813	59805.7	61.8937075333(16)	-1.9978974(51)	1.566(42)	24.13(65)	162	109/18	22
18	59889	60027	59958	59957.1	61.8912289268(14)	-1.9981564(29)	0.846(31)	13.11(48)	140	132/22	26
19	60070	60221	60145	60135.6	61.8880344209(9)	-1.9982364(18)	0.582(16)	9.03(25)	73.8	16.9/13	17
20	60224	60358	60291	60294.2	61.8855349303(12)	-1.9983872(23)	0.864(30)	13.39(46)	69.2	15.1/11	15
21	60401	60585	60492	60502.7	61.8820960295(51)	-1.9981842(48)	0.781(51)	12.10(79)	126	16.6/2	6
22	60600	60754	60686	60666.4	61.8787773846(19)	-1.9987440(57)	0.749(38)	11.59(58)	135	38.5/6	10
23	60771	60827	60799	60803.1	61.8768369527(25)	-1.998925(40)	[1] ^a	—	129	22.8/5	8

^a $\ddot{\nu}$ is fixed at 10^{-20} Hz s $^{-2}$ due to low number of TOAs and/or timespan too short to measure $\ddot{\nu}$. ^b No fit performed.

this 13-year period (Antonopoulou et al. 2018; Ferdman et al. 2018). NICER started regular monitoring observations of PSR J0537–6910 soon after its launch in mid-2017. Phase-connected timing models and 8 glitches measured with NICER data through 2020 April were presented in Ho et al. (2020b). Subsequent timing models through 2020 October, including 3 further glitches, and then through 2022 February, including 4 more glitches, were reported in Abbott et al. (2021a) and Ho et al. (2022), respectively. Here we report timing models using the remaining NICER data from 2022 March through 2025 June, with 8 new glitches detected during this period (first 6 of which are also reported in Zubieta et al. 2026). Tables 4 and 5 show timing models and glitch parameters derived from the complete NICER dataset from 2017 to 2025, including those given in our previous works above. We use our previous naming convention, where each segment is separated by a glitch and is labeled by glitch number, with segment 1 occurring after glitch 1, which is the first NICER-detected glitch. Figure 3 shows residuals of our best-fit timing models to all the NICER data, Figure 4 plots the spin-down rate $\dot{\nu}$ measured by RXTE and NICER since 1999, and Figure 5 displays glitch parameters $\Delta\nu$ and $\Delta\dot{\nu}$ for the 23 glitches measured using NICER. A best-fit linear decline for the long-term spin-down rate yields $\dot{\nu} = (-7.85 \pm 0.04) \times 10^{-22}$ Hz s $^{-2}$ and a braking index $n = -1.222 \pm 0.007$ calculated using ν and $\dot{\nu}$ from around the middle of the 25 years of RXTE and NICER observations. For a few glitches, an exponential recovery term is included in the glitch model [see equation (2)], but the presence of the recovery is not considered when characterising the intervals between glitches. A detailed study of exponential recoveries of glitches of PSR J0537–6910 is conducted in Zubieta et al. (2026).

As discussed in Ho et al. (2022, and references therein), the short-term spin-down behavior of PSR J0537–6910 (i.e., behavior between glitches) is very different from the long-term behavior seen in Figure 4. In particular, the interglitch braking index n_{ig} , calculated using the spin parameters of each segment between glitches (see Table 4), is non-negative and much greater than the canonical value of 3 that is predicted for conventional spin-down by electromagnetic dipole radiation at constant magnetic field and moment of inertia. This is illustrated in Figure 6, which shows n_{ig} measured using NICER and RXTE, with the latter values taken from Antonopoulou et al. (2018), and time since last glitch is the epoch of the segment minus the epoch of the corresponding glitch (e.g., time since glitch 23 = $60794 - 60762 = 32$ d). It is clear that large values of n_{ig} are measured for short times after a glitch and that small n_{ig} are measured after long post-glitch times. In other words, it appears there is recovery back to a rotational behavior that is characterized by a braking index $\lesssim 7$ after disruption by a glitch. Fits to an exponential decay yield decay timescales of 19–44 d, with a longer timescale for a lower asymptotic braking index (Ho et al. 2020b). Braking indices of 5 and 7 are expected for spin-down by gravitational wave quadrupole and r-mode emission, respectively.

Glitches of PSR J0537–6910 are unique in that the time to next glitch is correlated with the size of the preceding glitch (see also references in Section 1.1). This is illustrated in Figure 7. The correlation can be fit by time to next glitch = 50 d ($\Delta\nu/10 \mu\text{Hz} + 24$ d, in agreement with that found in Ho et al. (2020b, 2022)). This correlation enables prediction of when glitches will occur in PSR J0537–6910.

Because of the non-imaging wide field-of-view of NICER and bright X-ray emission from the surrounding region around

Table 5. Glitch parameters of PSR J0537–6910. Columns are glitch number and epoch and change in rotation phase and changes in spin frequency and its first two time derivatives at each glitch. Numbers in parentheses are 1σ uncertainty in last digit. Values for glitches 1–7, 8–10, and 11–15 are consistent with those given in Ho et al. (2020b), Abbott et al. (2021a), and Ho et al. (2022), respectively.

Glitch	Glitch epoch (MJD)	$\Delta\phi$ (cycle)	$\Delta\nu$ (μHz)	$\Delta\dot{\nu}$ ($10^{-13} \text{ Hz s}^{-1}$)	$\Delta\ddot{\nu}$ ($10^{-20} \text{ Hz s}^{-2}$)	$\Delta\nu_d$ (μHz)	τ_d (d)
1	58083 \pm 25	−0.016(8)	16.132(2)	−1.54(5)	—	—	—
2	58152 \pm 11	0.23(16)	36.026(44)	−1.48(20)	—	0.532(86)	6.3(25)
3	58363 \pm 14	0.167(50)	7.829(55)	−2.29(36)	5.4(11)	—	—
4	58424 \pm 2	−0.35(23)	25.33(28)	−2.1(12)	−5.1(20)	—	—
5	58566 \pm 5	−0.324(21)	9.205(16)	−0.890(51)	—	—	—
6	58637 \pm 8	0.029(19)	26.986(13)	−0.861(39)	−0.120(27) ^a	—	—
7	58807 \pm 3	0.310(22)	7.565(30)	−2.21(26)	4.88(95)	—	—
8	58868 \pm 5	−0.05(17)	23.95(13)	−2.20(48)	−5.23(77)	0.48(83)	5.1(28)
9	58993 \pm 3	0.06(12)	0.41(10)	−0.26(84)	—	—	—
10	59049 \pm 3	−0.209(11)	8.424(12)	−1.074(50)	—	—	—
11	59103 \pm 5	0.39(37)	33.81(32)	−1.26(83)	−3.15(94)	0.2(13)	9.2(29)
12	59285 \pm 2	−0.256(11)	7.8722(81)	−0.938(26)	—	—	—
13	59351 \pm 2	0.513(20)	12.272(34)	−0.79(22)	0.92(49)	—	—
14	59454 \pm 8	0.309(14)	16.604(10)	−1.712(38)	—	—	—
15	59522 \pm 8	−0.294(28)	22.062(16)	−0.519(46)	−0.202(23)	—	—
16	59692 \pm 5	−0.175(16)	5.835(14)	−0.857(61)	—	—	—
17	59741 \pm 5	−0.420(19)	15.400(16)	−1.062(69)	0.556(37)	—	—
18	59886 \pm 4	0.103(7)	24.3746(49)	−1.767(19)	−0.710(30)	—	—
19	60028 \pm 1	1.97(23)	34.00(10)	−1.02(16)	−0.39(12)	0.25(25)	29.7(46)
20	60223 \pm 1	0.224(7)	21.0960(21)	−0.706(23)	—	0.282(30)	33.1(52)
21	60379 \pm 22	0.386(60)	31.494(29)	−1.223(85)	−0.130(78)	—	—
22	60592 \pm 8	−0.244(32)	31.042(15)	−1.842(67)	−0.033(61)	—	—
23	60762 \pm 9	−0.352(18)	10.918(13)	−0.909(43)	—	—	—

^aIn the preceding segment, $\ddot{\nu}$ is fixed at $10^{-20} \text{ Hz s}^{-2}$ due to a low number of TOAs (see Table 2). $\Delta\ddot{\nu}$ is the difference between this fixed value and $\ddot{\nu}$ in the next segment.

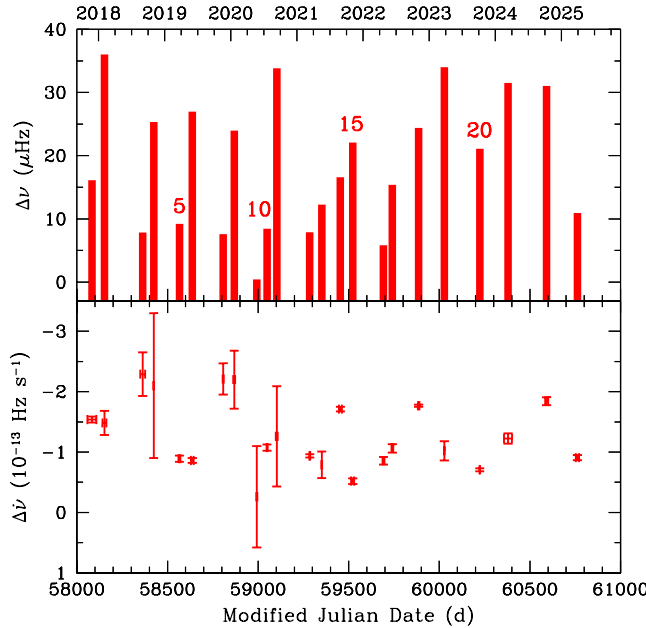


Figure 5. Glitch $\Delta\nu$ (top) and $\Delta\dot{\nu}$ (bottom) as functions of time. Errors in $\Delta\nu$ are 1σ uncertainty.

PSR J0537–6910, we do not perform spectral analyses of the NICER data here and leave this for future work. The X-ray spectrum of the pulsar has been studied previously. Chen et al. (2006, see also Townsley et al. 2006) fit the total (pulsed plus unpulsed or on plus

off-pulse) Chandra spectrum of PSR J0537–6910 with an absorbed power law model and found a hydrogen absorption column density $N_{\text{H}} = 5.6_{-0.3}^{+0.5} \times 10^{21} \text{ cm}^{-2}$, power law index $\Gamma = 1.73_{-0.06}^{+0.11}$, and unabsorbed 0.5–10 keV flux of $1.9 \times 10^{-12} \text{ erg s}^{-1} \text{ cm}^{-2}$, where uncertainties are at 90 percent confidence. Meanwhile, Kuiper & Hermsen (2015) derived the 0.7–250 keV pulsed flux spectrum of PSR J0537–6910 using RXTE and XMM-Newton data and by assuming an absorbed curved power law spectral model and modeling the pulse profiles as a function of energy.

Here we provide a more straightforward measurement of the pulsed spectrum at X-ray energies 3–79 keV using a 105 ks NuSTAR observation from 2016 (see Table 2). Note that Bamba et al. (2022) analyzed this same NuSTAR data, alongside Suzaku data, to determine the total (pulsar+pulsar wind nebula) spectrum at 1.5–79 keV but did not perform timing analysis to extract the pulsed spectrum of PSR J0537–6910. First, we follow the procedure described in Section 2.3 and measure a spin frequency $\nu = 61.93022931(7) \text{ Hz}$ at MJD 57678.64, where the 1σ uncertainty in the last digit is given in parentheses. Figure 8 shows the resulting 3–20 and >20 keV pulse profiles when the data are folded at this frequency, alongside the 1–7 keV pulse profile measured using NICER data. This spin frequency is $\sim 300 \mu\text{Hz}$ higher than the frequency predicted assuming the approximate pulsar spin-down rate during the time since the last RXTE data five years prior to the NuSTAR observation (see Figure 4). Such a deviation can be expected, given that PSR J0537–6910 likely underwent > 15 spin-up glitches during this time. Analogously, the NuSTAR frequency is $\sim 30 \mu\text{Hz}$ lower than the frequency extrapolated from the first NICER data. This is consistent with a few spin-up glitches during the intervening year between NuSTAR and NICER observations.

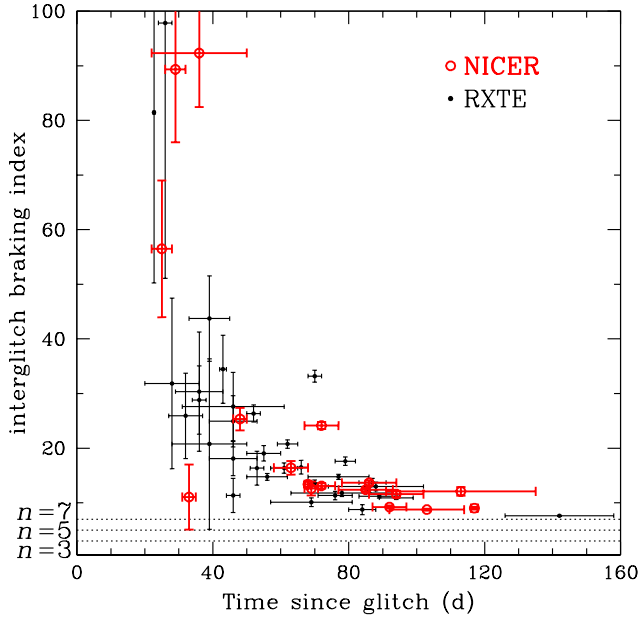


Figure 6. Interglitch braking index n_{ig} of PSR J0537–6910 calculated from spin parameters of each segment between glitches as a function of time since the last glitch. Large and small circles denote NICER and RXTE values, respectively (from Tables 4 and 5 and Antonopoulou et al. 2018). Errors in n_{ig} are 1σ . Horizontal dotted lines indicate braking index $n = 3, 5$, and 7 , which are expected for pulsar spin-down by electromagnetic dipole radiation, gravitational wave-emitting mountain, and gravitational wave-emitting r-mode oscillation, respectively.

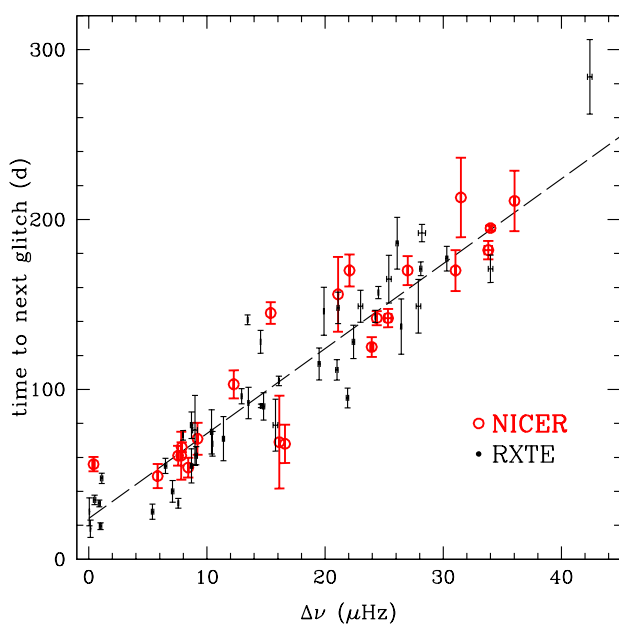


Figure 7. Correlation between time interval to the next glitch ΔT and size of glitch $\Delta\nu$ of PSR J0537–6910. Large and small circles denote NICER and RXTE values, respectively (from Table 5 and Antonopoulou et al. 2018). Errors in $\Delta\nu$ are 1σ . Dashed line shows linear fit result $\Delta T = 50$ d $(\Delta\nu/10 \mu\text{Hz}) + 24$ d.

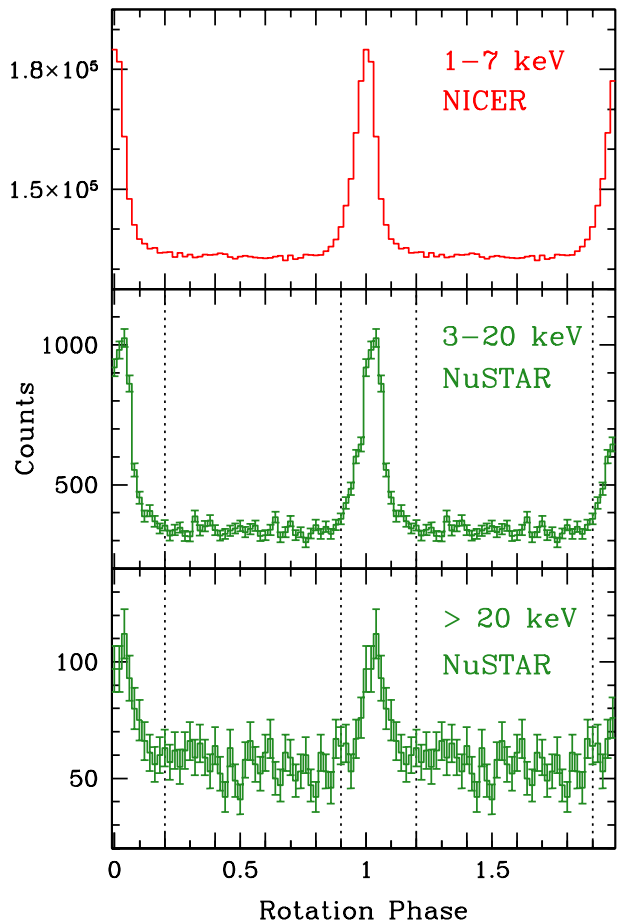


Figure 8. Pulse profile of PSR J0537–6910 from NICER data at 1–7 keV (top) and NuSTAR data at 3–20 keV (middle) and > 20 keV (bottom). Errors are 1σ uncertainty. Two rotation cycles are shown for clarity. Phase alignment between NICER and NuSTAR is arbitrary since datasets do not overlap. Dotted lines indicate phase ranges chosen for on-pulse (phase < 0.2 or > 0.9) and off-pulse ($0.2 < \text{phase} < 0.9$) NuSTAR spectra.

To extract pulsed spectra, we determine peak on-pulse emission as rotation phases below 0.2 or above 0.9 and off-pulse emission as phases outside the on-pulse ranges (see Figure 8). The off-pulse spectra are used as the background for the on-pulse spectra, such that the final pulsed spectra are the result of on minus off. We model the final pulsed spectra in Xspec (Arnaud 1996) using an absorbed power law, in particular tbabs with abundances from Wilms et al. (2000) and cross-sections from Verner et al. (1996) and powerlaw. We fix the absorption N_{H} to the value $7 \times 10^{21} \text{ cm}^{-2}$, based on our analysis below of the same Chandra data in Chen et al. (2006), where they determined the slightly lower value noted above. We find a best-fit $\Gamma = 1.62 \pm 0.05$ with $\chi^2/\text{dof} = 164/165$ and unabsorbed 2–10 keV flux of $(2.3 \pm 0.1) \times 10^{-12} \text{ erg s}^{-1} \text{ cm}^{-2}$ and 3–79 keV flux of $(7.8 \pm 0.4) \times 10^{-12} \text{ erg s}^{-1} \text{ cm}^{-2}$. Accounting for the on-pulse phase width of 0.3, the phase-averaged unabsorbed pulsed fluxes are $(6.9 \pm 0.3) \times 10^{-13} \text{ erg s}^{-1} \text{ cm}^{-2}$ for 2–10 keV and $(2.3 \pm 0.1) \times 10^{-12} \text{ erg s}^{-1} \text{ cm}^{-2}$ for 3–79 keV.

Since the best-fit power law index $\Gamma \approx 1.6$ for the pulsed component at 3–79 keV is similar to the $\Gamma \approx 1.7$ obtained by Chen et al. (2006) for the pulsed+unpulsed component at 0.5–10 keV, we test

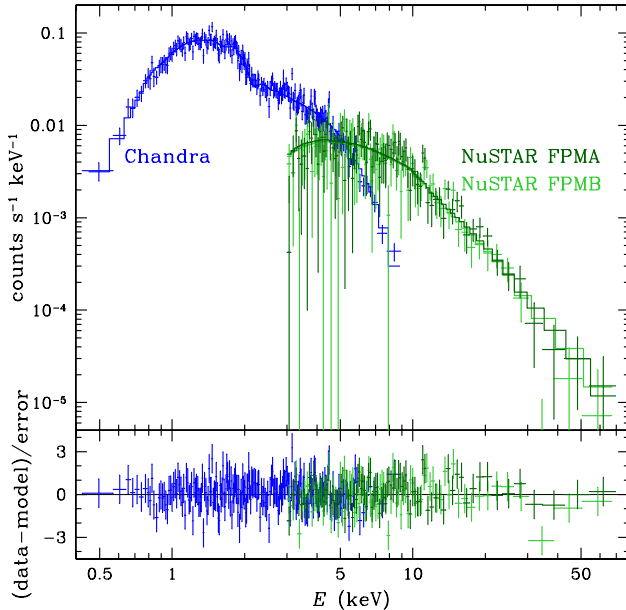


Figure 9. Pulsed spectra of PSR J0537–6910 from Chandra and NuSTAR FPMA and FPMB data. Top panel shows data with 1σ errors (crosses) and power law spectral model (solid lines). Bottom panel shows $\chi^2 = (\text{data}-\text{model})/\text{error}$.

whether a single power law could be used to describe the broadband (~ 0.3 –79 keV) pulsed spectrum of PSR J0537–6910. We use the same Chandra observation (see Table 2) and source and background regions to extract the pulsed+unpulsed spectrum as that used in Chen et al. (2006). For a joint spectral modeling of both the Chandra and NuSTAR data, we include an extra model fit parameter, `constant`, in addition to `tbabs` and `powerlaw`. This normalization parameter is allowed to vary for the Chandra spectrum but is fixed to 1 for the NuSTAR spectra. The variation of this normalization from unity for the Chandra spectrum can be interpreted as a combination of the contribution of the unpulsed component to the Chandra spectrum, assuming this contribution is energy-independent, and detector calibration uncertainties between Chandra and NuSTAR. We find a best-fit with $\chi^2/\text{dof} = 344/356$ that yields a Chandra normalization of 0.73 ± 0.04 , $N_{\text{H}} = (7.1 \pm 0.3) \times 10^{21} \text{ cm}^{-2}$, and $\Gamma = 1.67 \pm 0.03$. The phase-averaged unabsorbed 2–10 keV pulse flux is $(7.1 \pm 0.2) \times 10^{-13} \text{ erg s}^{-1} \text{ cm}^{-2}$, which is consistent with the fluxes derived from ASCA and RXTE data by Marshall et al. (1998) and RXTE and XMM-Newton data by Kuiper & Hermsen (2015). Figure 9 shows the NuSTAR pulsed spectra and the “derived” Chandra pulsed spectra, as well as our best-fit model.

3.3 PSR B0540–69

NICER observations of PSR B0540–69 began on 2017 July 25. Previous works reported timing models using NICER data from a relatively short time range of 2023 January 19 to May 3, supplemented by IXPE data (Xie et al. 2024), and from 2022 November 18 to 2023 December 25 (Tuo et al. 2024). In Espinoza et al. (2024), we presented results from our timing models using NICER data from the start of its observations on 2017 July 25 through 2024 July 29, supplemented by IXPE and Swift data. Here we provide the timing models and update these models to include all the effective NICER

data through 2025 May 20. Figure 10 shows timing residuals of the TOAs used to obtain our best-fit timing models, which are given in Table 6. Here the timing model segments for PSR B0540–69 are not separated by glitches, in contrast to the glitch-separated segments in the timing model for, e.g., PSR J0537–6910 given in Section 3.2. The segments are determined by periods over which a model that includes $\dot{\nu}$ provides a resonable fit to the data.

The latest data and longer term timing analysis continues to indicate the timing event that occurred around MJD 60139 was not a spin-down glitch as reported by Tuo et al. (2024) but a more subtle change in spin-down behavior (see Espinoza et al. 2024, for more details). Figure 11 shows the braking index n ($= \dot{\nu}\nu/\dot{\nu}^2$), calculated for each segment of the timing model given in Table 6, as a function of time. The slowly growing braking index measured by Espinoza et al. (2024) through early 2024 continues through 2025. We also see the effect of the timing event on the braking index measurement near that time.

3.4 PSR J1412+7922

NICER observations of PSR J1412+7922 began on 2017 September 15, and Bogdanov et al. (2019) reported a phase-connected timing model using the first year of data through 2018 October. Mereghetti et al. (2021) extended the timing model to 3.4 yr using NICER data through 2021 February, and Ho et al. (2022) further extended the model another year using data through 2022 February. More recently, Rigoselli et al. (2024) reported the 6.1 yr timing model using data through 2023 November. Here we complete the timing model using the remaining effective NICER data through 2025 April 23, covering a period of over 7.6 yr.

To construct a timing model that includes the pulsar’s position as a fit parameter, as done in Ho et al. (2022), we calculate 189 space-craft topocentric, not barycentric, TOAs from the dataset, and we fit these TOAs using PINT. In our timing analysis, we do not include the pulsar’s proper motion, as determined by Rigoselli et al. (2024) using Chandra data, so that we can obtain a position independent of their imaging analysis. The bottom panel of Figure 12 shows timing residuals of the topocentric TOAs used to obtain our best-fit timing model, which is given in Table 7. For comparison, we show in the top panel timing residuals from a TEMPO2 best-fit of the corresponding barycentric TOAs to a timing model that includes ν , $\dot{\nu}$, and $\ddot{\nu}$ but not $\ddot{\nu}$ and position; the worse fit and long timescale variations of the residuals are evident. We find that our position from timing is consistent with the Chandra astrometric imaging position from Rigoselli et al. (2024) of R.A. = $14^{\text{h}}12^{\text{m}}56\overset{\text{s}}{.}126(8)$ and decl. = $+79^{\circ}22'03\overset{\text{s}}{.}54(2)$ at MJD 60374, as well as the pulsar’s proper motion (see Section 1.1), and our uncertainty is about twice that of Chandra’s.

3.5 PSR J1811–1925

NICER monitoring of PSR J1811–1925 began with a few observations in 2021 September and then commenced in earnest in 2022 March. Here we report the timing model derived from all NICER data through 2025 May. Analysis of these data suggest PSR J1811–1925 suffers from timing noise. As a result, we find the TOAs are better modeled by dividing them into two epochs: TOAs obtained before the period in late 2023 when PSR J1811–1925 cannot be observed due to its proximity to the Sun in the sky and TOAs obtained after this period in early 2024, i.e., before about MJD 60227 and after about MJD 60390. Figure 13 shows residuals of our best-fit timing models for these two epochs, which are given in Table 8, and Figure 14 shows

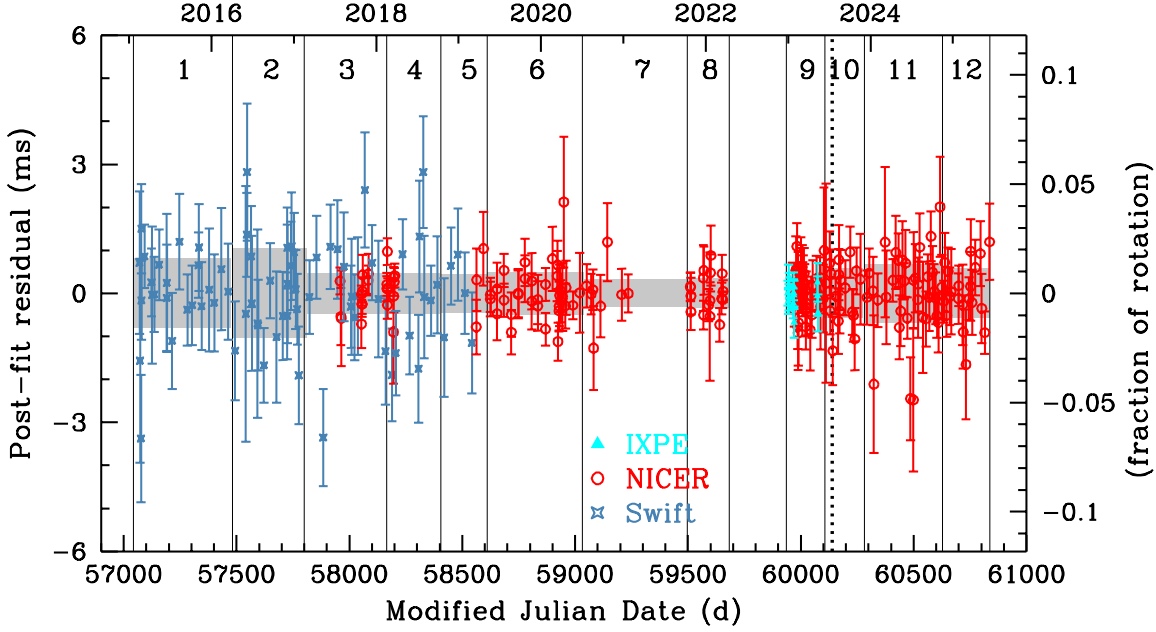


Figure 10. Timing residuals of PSR B0540–69 from a best-fit of IXPE (triangles), NICER (circles), and Swift (crosses) pulse times-of-arrival with the timing model given in Table 6 and RMS residuals illustrated by the shaded regions. Errors are 1σ uncertainty. Segments are denoted by vertical solid lines and labeled by numbers; overlaps of some segments are not indicated. Vertical dotted line at MJD 60139 denotes the occurrence of a timing event (see text for details).

Table 6. Timing parameters of PSR B0540–69. Columns are similar to those in Table 4. Numbers in parentheses are 1σ uncertainty in last digit. Position of R.A. = $05^{\text{h}}40^{\text{m}}11\overset{\text{s}}{.}202$, decl. = $-69^{\circ}19'54\overset{\text{s}}{.}17$ is from Hubble WFPC2 images (MJD 54272), with a 1σ uncertainty of $0\overset{\text{s}}{.}07$ (Mignani et al. 2010). Solar system ephemeris used is DE405.

Segment	Start (MJD)	End (MJD)	Epoch (MJD)	t_0 (MJD)	ν (Hz)	$\dot{\nu}$ (10^{-10} Hz s $^{-1}$)	$\ddot{\nu}$ (10^{-21} Hz s $^{-2}$)	n	RMS (μs)	χ^2/dof	TOAs
1	57044	57473	57430	57247.5	19.6930733748(23)	-2.5286496(38)	0.090(26)	0.0277(80)	811	14.0/19	23
2	57482	57810	57620	57649.1	19.6889224954(17)	-2.5284950(28)	0.805(95)	0.248(29)	1043	18.9/17	21
3	57800	58163	58000	57976.1	19.68062121257(74)	-2.5282227(14)	2.041(41)	0.628(13)	475	25.3/21	25
4	58165	58400	58300	58266.7	19.6740689746(14)	-2.5274940(69)	2.58(15)	0.795(47)	481	27.5/16	20
5	58406	58881	58650	58654.0	19.66642738628(57)	-2.52646402(47)	3.485(13)	1.0736(40)	448	9.75/13	17
6	58611	59036	58830	58834.9	19.66249864699(53)	-2.52594021(57)	3.255(16)	1.0031(49)	495	21.5/20	24
7	59033	59550	59280	59235.8	19.6526803925(19)	-2.52455830(52)	3.798(30)	1.1710(93)	313	3.93/6	10
8	59497	59683	59610	59591.3	19.6454838675(17)	-2.5234484(99)	3.52(43)	1.09(13)	342	12.9/11	15
9	59935	60107	60020	60021.6	19.63654744724(73)	-2.5219243(20)	4.58(15)	1.414(46)	345	33.6/44	48
10	60107	60276	60200	60197.5	19.6326257165(19)	-2.5213478(85)	5.99(54)	1.85(17)	577	15.1/14	18
11	60282	60630	60470	60458.3	19.62674530613(83)	-2.52021134(79)	4.559(34)	1.409(10)	683	33.9/31	35
12	60628	60836	60730	60731.9	19.6210851128(15)	-2.5190981(23)	5.25(16)	1.623(50)	577	15.9/16	20

the pulse profile at 2.5–8 keV from the combined NICER observations. We note that we are able to construct a single timing model for the entire period of NICER observations, but such a model requires two additional spin terms (fourth and fifth time derivatives of ν) and yields a best-fit with RMS of 2.15 ms and $\chi^2/\text{dof} = 90/35$.

3.6 PSR J1813–1749

Unlike the rotation phase-connected (coherent) timing models for the other pulsars presented in this work, the timing model for PSR J1813–1749 is incoherent, i.e., $\dot{\nu}$ is determined by a best-fit to a simple linear model for the change of ν over time. This is be-

cause of the sparse number of individual measurements of the spin frequency such that a phase-connected model is not possible.

We report new spin frequency measurements of PSR J1813–1749 using three recent Chandra CC observations taken in 2024 and 2025 (see Table 2). Analysis of these data yield $\nu = 22.3416735(50)$ Hz on MJD 60403.03, and $\nu = 22.3406187(47)$ Hz on MJD 60590.78 and $\nu = 22.3396994(42)$ Hz on MJD 60758.00, where the 1σ uncertainty in the last digit is given in parentheses. These measurements are shown in Figure 15, as well as previous ones using Chandra and XMM-Newton (Halpern et al. 2012; Ho et al. 2022), Green Bank Telescope at radio wavelengths (Camilo et al. 2021), NICER (Ho et al. 2020a), and NuSTAR (Ho et al. 2022). Fitting a simple linear decline in spin frequency yields a best-fit spin-down rate

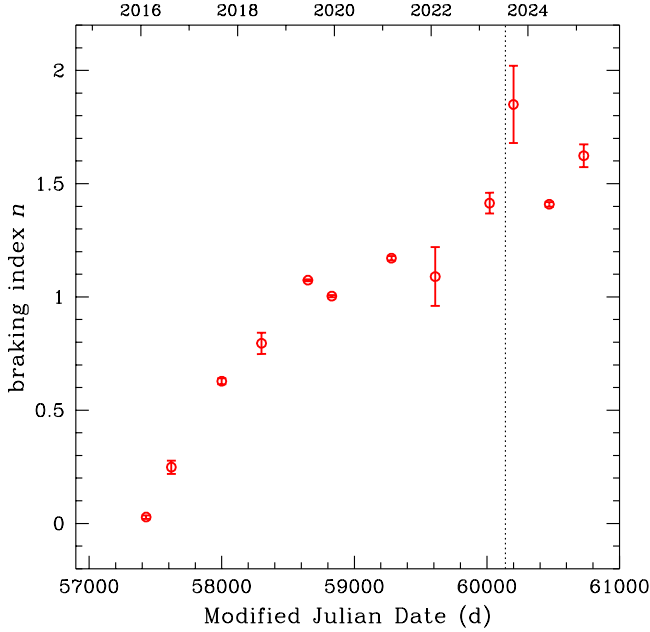


Figure 11. Evolution of braking index $n = \dot{v}v/\dot{v}^2$ of PSR B0540-69 as measured during each segment of the timing model given in Table 6. Errors are 1σ uncertainty. Vertical dotted line at MJD 60139 denotes the occurrence of a timing event (see text for details).

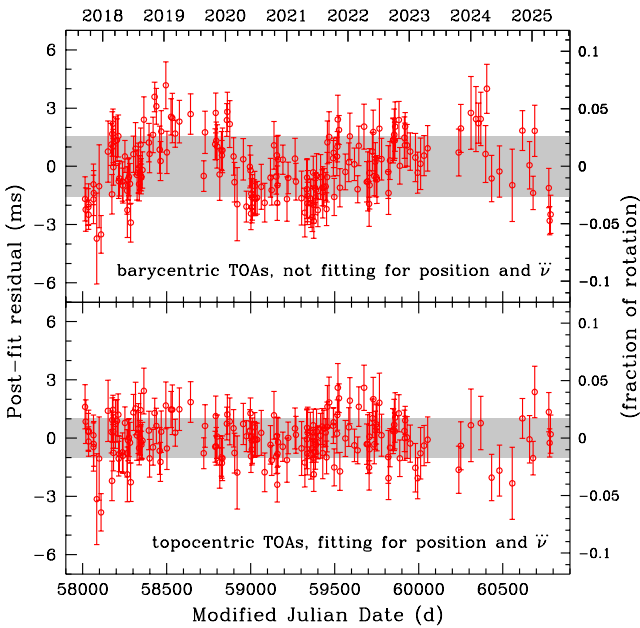


Figure 12. Top panel shows timing residuals of PSR J1412+7922 from a best-fit of NICER barycentric pulse times-of-arrivals with a timing model that includes \dot{v} but not \ddot{v} nor position. Bottom panel shows timing residuals of PSR J1412+7922 from a best-fit of NICER topocentric TOAs with the timing model given in Table 7. Errors are 1σ uncertainty. The RMS residuals are illustrated by the shaded regions between ± 1.55 ms (top) and between ± 1.03 ms (bottom).

Table 7. Timing parameters of PSR J1412+7922. Numbers in parentheses are 1σ uncertainty in last digit. Position epoch is MJD 58750. Proper motion is not taken into account in the fit.

Parameter	Value
R.A. α (J2000)	14 ^h 12 ^m 56 ^s 035(19)
Decl. δ (J2000)	+79°22'03"518(43)
Solar system ephemeris	DE405
Range of dates (MJD)	58014–60784
Epoch (MJD TDB)	59400
t_0 (MJD)	58815.3
Frequency v (Hz)	16.89205540623(5)
Freq. 1st derivative \dot{v} (Hz s ⁻¹)	-9.420861(24) $\times 10^{-13}$
Freq. 2nd derivative \ddot{v} (Hz s ⁻²)	-2.6597(33) $\times 10^{-23}$
Freq. 3rd derivative \dddot{v} (Hz s ⁻³)	2.52(22) $\times 10^{-32}$
RMS residual (ms)	1.030
χ^2/dof	201.8/182
Number of TOAs	189

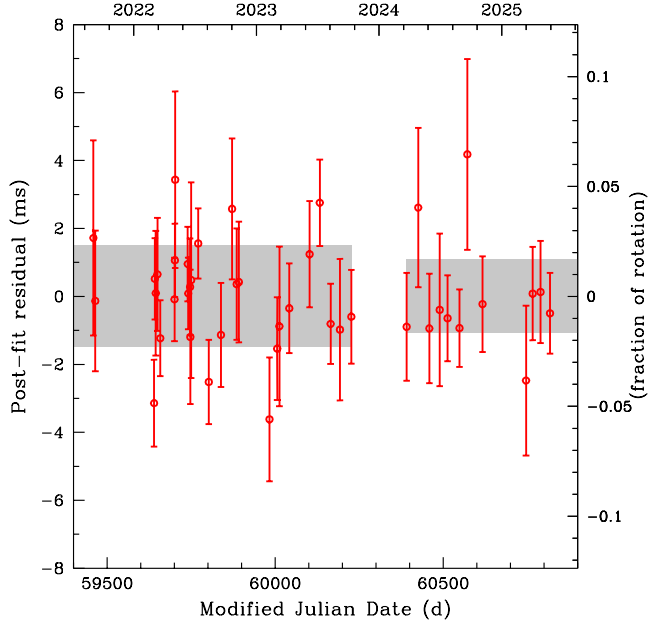


Figure 13. Timing residuals of PSR J1811-1925 from two separate best-fits of NICER pulse times-of-arrival with the timing models given in Table 8. Errors are 1σ uncertainty. The RMS residual of each best-fit is illustrated by the shaded regions between ± 1.49 ms before MJD 60230 and between ± 1.08 ms after MJD 60390.

$\dot{v} = (-6.34424 \pm 0.00064) \times 10^{-11}$ Hz s⁻¹. Table 9 presents the resulting 16 yr timing model. Residuals from the timing model, as seen in the bottom panel of Figure 15, suggest PSR J1813-1749 undergoes glitches with sizes as large as a few tens of μ Hz, which are typical for young pulsars.

We also attempt to measure the pulsed spectrum of PSR J1813-1749 by combining all previous Chandra CC data. This spectrum is obtained by first using measurements of the spin parameters for each individual observation and extracting photons during the rotation phases around the peak of the pulse profile (on-pulse) and away from the peak (off-pulse). Pulsed spectra are then determined by subtracting the off-pulse emission from the on-pulse emission. We then combine all the Chandra pulsed spectra into a single spectrum. Unfortunately, the resulting pulsed spectrum has poor photon

Table 8. Timing parameters of PSR J1811–1925. Numbers in parentheses are 1σ uncertainty in last digit. The position is from a Chandra ACIS-S image (MJD 51762), with a 1σ uncertainty of $0''.6$ (Kaspi et al. 2001).

Parameter	Value
R.A. α (J2000)	18 ^h 11 ^m 29 ^s .22
Decl. δ (J2000)	−19°25'27''.6
Solar system ephemeris	DE405
Range of dates (MJD)	59459–60230
Epoch (MJD TDB)	59701
t_0 (MJD)	59871.5
Frequency ν (Hz)	15.4544586828(11)
Freq. 1st derivative $\dot{\nu}$ (Hz s ^{−1})	$−1.0669215(75) \times 10^{−11}$
Freq. 2nd derivative $\ddot{\nu}$ (Hz s ^{−2})	$−2.64(16) \times 10^{−22}$
Freq. 3rd derivative $\dddot{\nu}$ (Hz s ^{−3})	$−5.6(12) \times 10^{−30}$
RMS residual (ms)	1.49
χ^2/dof	31.8/25
Number of TOAs	30
Range of dates (MJD)	60390–60818
Epoch (MJD TDB)	60458
t_0 (MJD)	60512.8
Frequency ν (Hz)	15.4537601837(19)
Freq. 1st derivative $\dot{\nu}$ (Hz s ^{−1})	$−1.068594(86) \times 10^{−11}$
Freq. 2nd derivative $\ddot{\nu}$ (Hz s ^{−2})	$−8.7(18) \times 10^{−22}$
Freq. 3rd derivative $\dddot{\nu}$ (Hz s ^{−3})	$5.2(13) \times 10^{−29}$
RMS residual (ms)	1.08
χ^2/dof	5.92/7
Number of TOAs	12

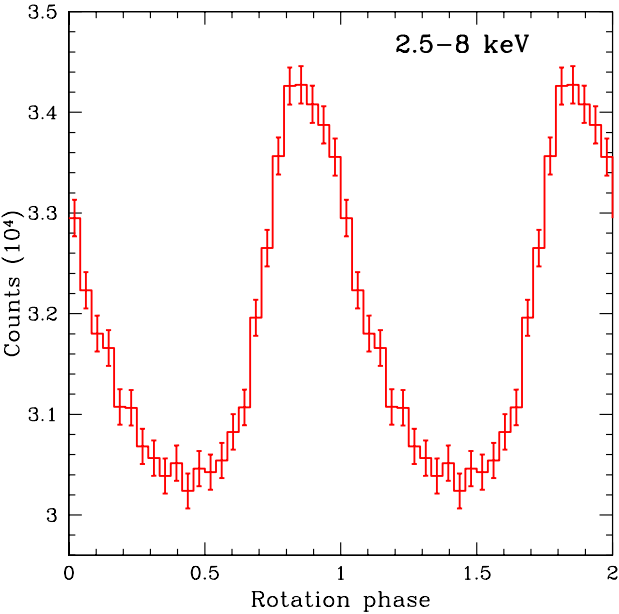


Figure 14. Pulse profile of PSR J1811–1925 from NICER data at 2.5–8 keV. Errors are 1σ uncertainty. Two rotation cycles are shown for clarity.

statistics, even when using a different extraction region, and thus we do not show it nor fit it with spectral models.

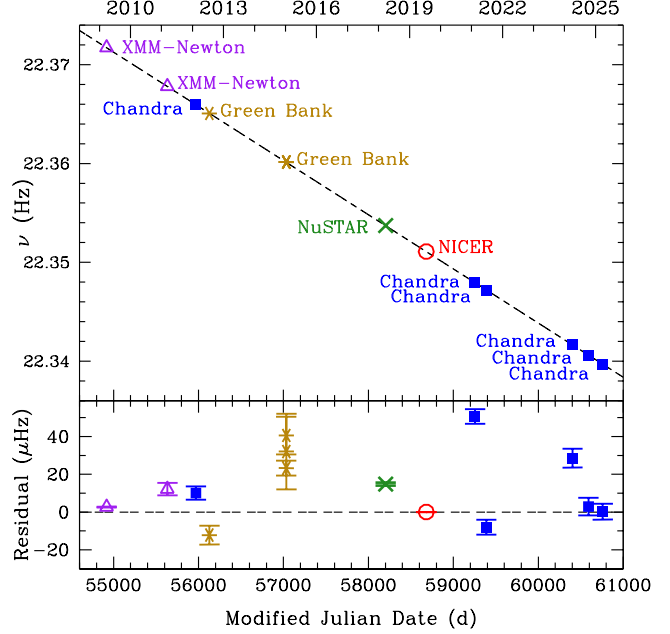


Figure 15. Spin frequency ν of PSR J1813–1749 (top) and difference between best-fit linear model and data (bottom) as functions of time. Errors are 1σ uncertainty. Measurements of ν are made using XMM-Newton (triangles), Chandra (squares), Green Bank Telescope in radio (stars), NuSTAR (cross), and NICER (circle). Dashed line shows a linear fit of all ν measurements with best-fit $\dot{\nu} = −6.3442 \times 10^{−11}$ Hz s^{−1}.

Table 9. Incoherent timing parameters of PSR J1813–1749. Numbers in parentheses are 1σ uncertainty in last digit. The position is from VLA data (MJD 58119), with uncertainties of $\sim 0''.009$ and $\sim 0''.13$, and proper motion has uncertainties of 3.7 and 6.7 mas yr^{−1} in $\mu_\alpha \cos \delta$ and μ_δ , respectively (Dzib & Rodríguez 2021).

Parameter	Value
R.A. α (J2000)	18 ^h 13 ^m 35 ^s .173
Decl. δ (J2000)	−17°49'57''.75
Solar system ephemeris	DE405
Range of dates (MJD)	54918.14–60758.00
Epoch (MJD TDB)	58681.04
Frequency ν (Hz)	22.3510838(2)
Freq. 1st derivative $\dot{\nu}$ (Hz s ^{−1})	$−6.3442(6) \times 10^{−11}$
Proper motion $\mu_\alpha \cos \delta$ (mas yr ^{−1})	−5.0
Proper motion μ_δ (mas yr ^{−1})	−13.2

3.7 PSR J1849–0001

NICER observations of PSR J1849–0001 began on 2018 February 13, and Bogdanov et al. (2019) reported a 1.5-year phase-connected timing model using the first 7 months of NICER data as well as a Swift observation from 2017 March. Ho et al. (2022) extended the timing model to 4.7 yr using NICER data through 2021 November. Kim et al. (2024) further extended the timing model by about 8 months using data through 2022 July. Here we complete the timing model using the remaining effective NICER data through 2025 June 8, covering a period of 7.3 yr that PSR J1849–0001 was observed by NICER.

As done for PSR J1412+7922 in Section 3.4, we seek to construct a timing model that includes the pulsar's position as a fit parameter. Thus we calculate 65 spacecraft topocentric TOAs from the dataset before the glitch that occurred sometime between 2024 April 12 and

Table 10. Timing parameters of PSR J1849–0001. Numbers in parentheses are 1σ uncertainty in last digit. Position epoch is MJD 55885. The middle column gives a timing model derived in two segments separated by the glitch on MJD 60428; the first segment covers MJD 58166–60413, includes position as a fit parameter, and uses topocentric TOAs, while the second segment covers MJD 60469–60835 and uses barycentric TOAs. The right column gives a timing model, including parameters of the glitch, derived using only barycentric TOAs covering MJD 58923–60835.

Parameter	Value	Value
R.A. α (J2000)	$18^{\text{h}}49^{\text{m}}01^{\text{s}}.6194(26)$	
Decl. δ (J2000)	$-00^{\circ}01'17''.445(99)$	
Solar system ephemeris	DE421	
Range of dates (MJD)	58166–60413	
Epoch (MJD TDB)	59289	
t_0 (MJD)	59289.3	
Frequency ν (Hz)	25.9581535113(2)	
Freq. 1st derivative $\dot{\nu}$ (Hz s $^{-1}$)	$-9.533059(9) \times 10^{-12}$	
Freq. 2nd derivative $\ddot{\nu}$ (Hz s $^{-2}$)	$5.12(9) \times 10^{-23}$	
Freq. 3rd derivative $\dddot{\nu}$ (Hz s $^{-3}$)	$-5.6(29) \times 10^{-32}$	
Freq. 4th derivative $\ddot{\ddot{\nu}}$ (Hz s $^{-4}$)	$-1.03(34) \times 10^{-38}$	
Freq. 5th derivative (Hz s $^{-5}$)	$-7.6(7) \times 10^{-46}$	
Freq. 6th derivative (Hz s $^{-6}$)	$5.4(9) \times 10^{-53}$	
RMS residual (μ s)	432	
χ^2/dof	81.9/55	
Number of TOAs	65	
Glitch epoch (MJD)		60428 ± 15
$\Delta\phi$		$-0.16(96)$
$\Delta\nu$ (Hz)		$4.3841(42) \times 10^{-5}$
$\Delta\dot{\nu}$ (Hz s $^{-1}$)		$-9.11(26) \times 10^{-14}$
$\Delta\ddot{\nu}$ (Hz s $^{-2}$)		$6.61(89) \times 10^{-22}$
$\Delta\nu_d$ (Hz)		$5.5(52) \times 10^{-7}$
τ_d (d)		30
Range of dates (MJD)	60469–60835	58923–60835
Epoch (MJD TDB)	60651	60428
t_0 (MJD)	60617.3	59869.2
Frequency ν (Hz)	25.9570741758(13)	25.9572155718(10)
Freq. 1st derivative $\dot{\nu}$ (Hz s $^{-1}$)	$-9.60605(53) \times 10^{-12}$	$-9.529343(68) \times 10^{-12}$
Freq. 2nd derivative $\ddot{\nu}$ (Hz s $^{-2}$)	$1.043(42) \times 10^{-21}$	$2.49(26) \times 10^{-23}$
Freq. 3rd derivative $\dddot{\nu}$ (Hz s $^{-3}$)	$-1.21(23) \times 10^{-28}$	$-2.54(41) \times 10^{-30}$
RMS residual (μ s)	437	508
χ^2/dof	8.54/6	80.6/39
Number of TOAs	11	49

May 12 (MJD 60412.6–60442.9) (Kuiper et al. 2024). We fit these TOAs using PINT. We do not include any proper motion of the pulsar since a recent analysis comparing a Chandra 2012 ACIS-S image and a 2021 ACIS-I image yielded a position change smaller than the uncertainties (Gagnon et al. 2024). Meanwhile, since the post-glitch epoch covered by NICER data is short and covers only 1 yr, we follow our more standard procedure and calculate 11 barycentric TOAs from the post-glitch data and fit these using TEMPO2 with a model that only includes frequency time derivatives through $\ddot{\nu}$ and does not include position.

Figure 16 shows timing residuals of the TOAs used to obtain our best-fit timing model, which is given in middle column of Table 10. We find that our position from timing is consistent with the Chandra HRC-S imaging position from Kuiper & Hermse (2015) of R.A. = $18^{\text{h}}49^{\text{m}}01^{\text{s}}.632$ and decl. = $-00^{\circ}01'17''.45$ at MJD 55885, which has a 90 percent confidence level uncertainty of $0''.6$. It is noteworthy that our timing position, with an uncertainty of $0''.11$, is now more accurate than the one from imaging.

To more accurately measure the glitch parameters, we perform a second fit using barycentric TOAs and restrict the timing model to terms up to $\ddot{\nu}$. We are unable to obtain a single timing model covering

the entire 7 years of NICER data and therefore only use data since 2020 March 15 (MJD 58923). The best-fit values are given in the right column of Table 10, including those for the glitch. The glitch magnitude, $\Delta\nu = 43.8 \mu\text{Hz}$ and $\Delta\nu/\nu = 1.69 \times 10^{-6}$, is among the largest observed and comparable to those seen in the Vela pulsar and PSR J0537–6910 (see, e.g., Figure 5 and Fuentes et al. 2017). We find the decay timescale τ_d has an uncertainty of ± 7 d.

Finally, Figure 17 shows the pre-glitch evolution of $\dot{\nu}$ and its residual relative to a model that includes an exponential decay, although there does not appear to be evidence for a large glitch within 2000 d before the start of our NICER observations. The spin-down values $\dot{\nu}$ shown here are calculated using at least 10 TOAs from overlapping intervals at least 300 days long with a varying $\dot{\nu}$, and each interval was moved by 5 days at each stride (see Espinoza et al. 2024). One can see the change of $\dot{\nu}$ over time and its oscillatory and growing in amplitude deviation from the model with time. This illustrates the long-term timing noise present in the spin evolution of PSR J1849–0001 and the need for higher-order spin frequency time derivatives in its timing model.

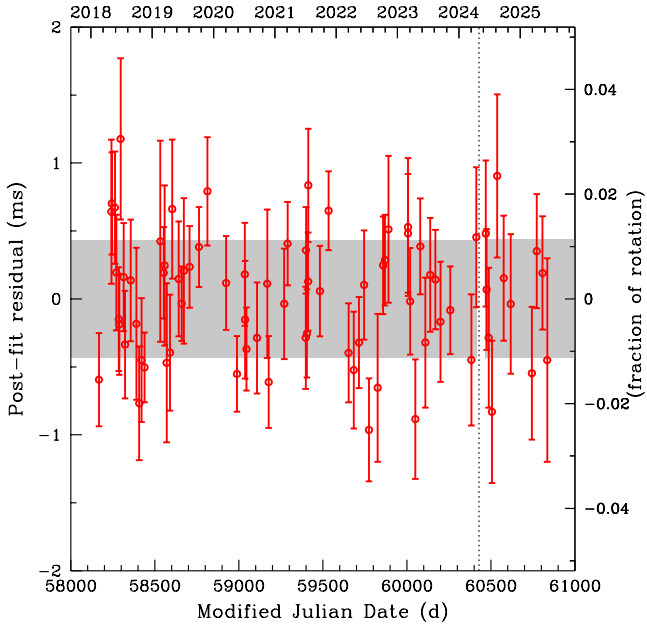


Figure 16. Timing residuals of PSR J1849–0001 from two separate best-fits of NICER pulse times-of-arrival, topocentric TOAs before the glitch and barycentric TOAs after the glitch, with the timing models given in the middle column of Table 10. Errors are 1σ uncertainty. The vertical dotted line indicates the approximate time of a spin-up glitch (MJD 60428). The RMS residual of each best-fit is illustrated by the shaded regions between ± 0.432 ms before the glitch and between ± 0.437 ms after the glitch.

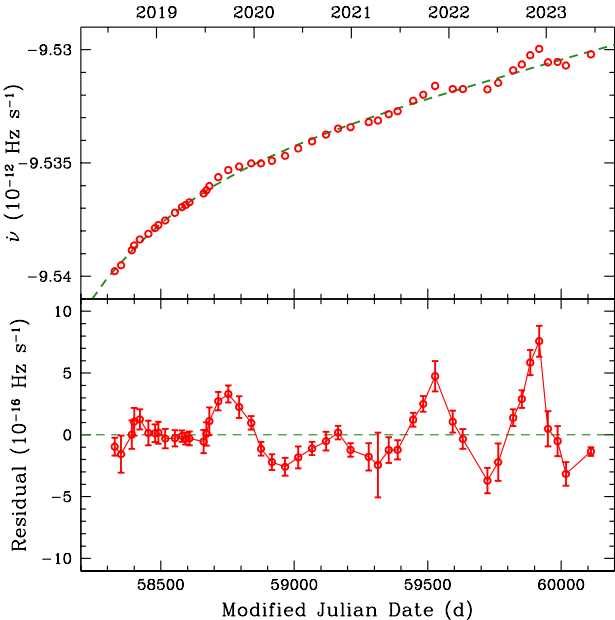


Figure 17. Top panel shows spin-down rate \dot{v} of PSR J1849–0001 calculated from overlapping intervals at least 300 days long (see text for details). The dashed line is for a model that includes \ddot{v} and an exponential decay with a ~ 1 yr timescale. Bottom panel shows difference between the data and model. Errors are 1σ uncertainty.

4 DISCUSSION

We reported here the years-long timing models for seven young energetic pulsars. Six of the timing models are rotation phase-connected and make use of all the data NICER collected on these pulsars during its 8 years of operation. For PSR J0058–7218, we detected its first three glitches in only 3.5 years of observation. It would be interesting to know if its glitching behavior shows any similarities to that of the Big Glitcher, PSR J0537–6910. For PSR J0537–6910, NICER data enabled detection of 23 glitches in 8 years, comparable to the 45 glitches in 13 years found using RXTE. These glitches continue to show evidence for their predictability. We also measured for the first time the spin pulsations and pulsed spectrum of PSR J0537–6910 using NuSTAR data. For PSR B0540–69, we provide its timing model over the past 10 years using a combination of IXPE, NICER, and Swift data and see that its braking index n has been growing over this decade from $n \approx 0$ to 1.6 as of mid-2025. For PSR J1412+7922 and PSR J1849–0001, the more than 7 years of NICER monitoring enabled measurements of their position from timing to accuracies comparable to that obtained from imaging.

For all seven pulsars studied here, their timing models are crucial for ongoing efforts to detect gravitational waves emitted by pulsars. These gravitational waves are continuous signals that can be emitted for the entire lifetime of a pulsar (see Haskell & Bejger 2023; Riles 2023; Wette 2023, for reviews). The frequency range of current ground-based gravitational wave detectors means that they are only sensitive to fast-spinning pulsars, and the most sensitive searches are those targeting pulsars that have an accurate timing model like those presented here. In fact, the timing models for the seven pulsars presented here and in previous works have already been used to search for gravitational waves in LIGO/Virgo/KAGRA data (Abbott et al. 2021a,b, 2022a,b; Abac et al. 2025).

Finally, it is important to emphasize that five of our seven pulsars are only observed as pulsars in the X-ray and thus their timing models necessitate regular monitoring by sensitive X-ray telescopes with fast and accurate timing capabilities, such as NICER. As an example, we searched for but did not detect pulsed emission from PSR J1811–1925 using Fermi-LAT data, like the non-detections of PSR J1412+7922 and PSR J1849–0001 described in Ho et al. (2022); we also reported in that work a possible detection of PSR J0058–7218 in Fermi-LAT data, but our much longer time baseline now no longer supports detection. Potential new general purpose X-ray telescopes, such as AXIS (Reynolds et al. 2024), could be invaluable in this regard if they possess an observing mode that utilizes a subarray and/or fast readout. The capability to obtain timing models for X-ray pulsars is required for the most sensitive searches for gravitational waves using the next generation gravitational wave detectors being developed for the 2030s, such as Cosmic Explorer (Evans et al. 2021) and Einstein Telescope (Maggiore et al. 2020).

ACKNOWLEDGEMENTS

WCGH thanks Paul Ray for discussions on timing analyses and George Younes for discussions on NuSTAR data analysis. WCGH acknowledges support through grants 80NSSC22K1305, 80NSSC24K1195, and 80NSSC25K0085 from NASA and Chandra award SAO GO4-25038X. Chandra grants are issued by the Chandra X-ray Center (CXC), which is operated by the Smithsonian Astrophysical Observatory for and on behalf of NASA under contract NAS8-03060. CME acknowledges support from ANID/FONDECYT, grant 1211964. TL acknowledges financial support from the Haverford Koshland Integrated Natural Sciences Center

(KINSC). BW acknowledges financial support from the Boughn-Gollub-Partridge Fund at Haverford College. SG acknowledges the support of the CNES.

This research made use of data obtained from the Chandra Data Archive and the Chandra Source Catalog, and software provided by the Chandra X-ray Center (CXC) in the application packages CIAO and Sherpa. This work is supported by NASA through the NICER mission and the Astrophysics Explorers Program and uses data and software provided by the High Energy Astrophysics Science Archive Research Center (HEASARC), which is a service of the Astrophysics Science Division at NASA/GSFC and High Energy Astrophysics Division of the Smithsonian Astrophysical Observatory. This research made use of data from the NuSTAR mission, a project led by the California Institute of Technology, managed by the Jet Propulsion Laboratory, and funded by the NASA. Data analysis was performed using the NuSTAR Data Analysis Software (NuSTARDAS), jointly developed by the ASI Science Data Center (SSDC, Italy) and the California Institute of Technology (USA). This work made extensive use of the NASA Astrophysics Data System (ADS) Bibliographic Services and the arXiv.

DATA AVAILABILITY

Data underlying this article will be shared on reasonable request to the corresponding author.

REFERENCES

Abac A. G., et al., 2025, [ApJ](#), **983**, 99

Abbott R., et al., 2021a, [ApJ](#), **913**, L27

Abbott R., et al., 2021b, [ApJ](#), **922**, 71

Abbott R., et al., 2022a, [ApJ](#), **932**, 133

Abbott R., et al., 2022b, [ApJ](#), **935**, 1

Agazie G., et al., 2023, [ApJ](#), **951**, L8

Antonopoulou D., Espinoza C. M., Kuiper L., Andersson N., 2018, [MNRAS](#), **473**, 1644

Antonopoulou D., Haskell B., Espinoza C. M., 2022, [Reports on Progress in Physics](#), **85**, 126901

Arias M., et al., 2022, [A&A](#), **667**, A71

Arnaud K. A., 1996, in Jacoby G. H., Barnes J., eds, Astronomical Society of the Pacific Conference Series Vol. 101, Astronomical Data Analysis Software and Systems V. p. 17

Bamba A., Shibata S., Tanaka S. J., Mori K., Uchida H., Terada Y., Ishizaki W., 2022, [PASJ](#), **74**, 1186

Bogdanov S., et al., 2019, [ApJ](#), **877**, 69

Borkowski K. J., Reynolds S. P., Roberts M. S. E., 2016, [ApJ](#), **819**, 160

Brogan C. L., Gaensler B. M., Gelfand J. D., Lazendic J. S., Lazio T. J. W., Kassim N. E., McClure-Griffiths N. M., 2005, [ApJ](#), **629**, L105

Camilo F., Ransom S. M., Halpern J. P., Roshi D. A., 2021, [ApJ](#), **917**, 67

Chen Y., Wang Q. D., Gotthelf E. V., Jiang B., Chu Y.-H., Gruendl R., 2006, [ApJ](#), **651**, 237

De Luca A., 2017, in Journal of Physics Conference Series. p. 012006 ([arXiv:1711.07210](#)), doi:10.1088/1742-6596/932/1/012006

Dzib S. A., Rodríguez L. F., 2021, [ApJ](#), **923**, 228

Espinoza C. M., Kuiper L., Ho W. C. G., Antonopoulou D., Arzoumanian Z., Harding A. K., Ray P. S., Younes G., 2024, [ApJ](#), **973**, L39

Evans M., et al., 2021, [arXiv e-prints](#), p. arXiv:2109.09882

Ferdman R. D., Archibald R. F., Gourgouliatos K. N., Kaspi V. M., 2018, [ApJ](#), **852**, 123

Fermi LAT Collaboration et al., 2015, [Science](#), **350**, 801

Fruscione A., et al., 2006, in Silva D. R., Doxsey R. E., eds, Society of Photo-Optical Instrumentation Engineers (SPIE) Conference Series Vol. 6270, Society of Photo-Optical Instrumentation Engineers (SPIE) Conference Series. p. 62701V, doi:10.1117/12.671760

Fuentes J. R., Espinoza C. M., Reisenegger A., Shaw B., Stappers B. W., Lyne A. G., 2017, [A&A](#), **608**, A131

Gagnon S., Kargaltsev O., Klingler N., Hare J., Yang H., Lange A., Eagle J., 2024, [ApJ](#), **968**, 67

Gendreau K. C., et al., 2016, in den Herder J.-W. A., Takahashi T., Bautz M., eds, Society of Photo-Optical Instrumentation Engineers (SPIE) Conference Series Vol. 9905, Space Telescopes and Instrumentation 2016: Ultraviolet to Gamma Ray. p. 99051H, doi:10.1117/12.2231304

Gotthelf E. V., Halpern J. P., 2009, [ApJ](#), **700**, L158

Gotthelf E. V., Halpern J. P., Terrier R., Mattana F., 2011, [ApJ](#), **729**, L16

Graczyk D., et al., 2020, [ApJ](#), **904**, 13

Greco E., Rigoselli M., Mereghetti S., Bocchino F., Miceli M., Sapienza V., Orlando S., 2025, [A&A](#), **701**, A43

HEASARC 2014, HEAsoft: Unified Release of FTOOLS and XANADU, Astrophysics Source Code Library, record ascl:1408.004

Halpern J. P., Gotthelf E. V., 2015, [ApJ](#), **812**, 61

Halpern J. P., Gotthelf E. V., Camilo F., 2012, [ApJ](#), **753**, L14

Halpern J. P., Bogdanov S., Gotthelf E. V., 2013, [ApJ](#), **778**, 120

Haskell B., Bejger M., 2023, [Nature Astronomy](#), **7**, 1160

Ho W. C. G., et al., 2020a, [MNRAS](#), **498**, 4396

Ho W. C. G., et al., 2020b, [MNRAS](#), **498**, 4605

Ho W. C. G., et al., 2022, [ApJ](#), **939**, 7

Hobbs G. B., Edwards R. T., Manchester R. N., 2006, [MNRAS](#), **369**, 655

Johnston S., Romani R. W., 2003, [ApJ](#), **590**, L95

Kaspi V. M., Roberts M. E., Vasisht G., Gotthelf E. V., Pivovaroff M., Kawai N., 2001, [ApJ](#), **560**, 371

Kilpatrick C. D., Bieging J. H., Rieke G. H., 2016, [ApJ](#), **816**, 1

Kim C., et al., 2024, [ApJ](#), **960**, 78

Kuiper L., Hermsen W., 2009, [A&A](#), **501**, 1031

Kuiper L., Hermsen W., 2015, [MNRAS](#), **449**, 3827

Kuiper L., Ho W. C. G., Espinoza C. M., Arzoumanian Z., Gendreau K., Bogdanov S., Guillot S., 2024, The Astronomer's Telegram, **16691**, 1

Luo J., et al., 2021, [ApJ](#), **911**, 45

Madsen K. K., Fryer C. L., Grefenstette B. W., Lopez L. A., Reynolds S., Zoglauer A., 2020, [ApJ](#), **889**, 23

Maggiore M., et al., 2020, [J. Cosmology Astropart. Phys.](#), **2020**, 050

Maitra C., Ballet J., Filipović M. D., Haberl F., Tiengo A., Grieve K., Roper Q., 2015, [A&A](#), **584**, A41

Maitra C., Esposito P., Tiengo A., Ballet J., Haberl F., Dai S., Filipović M. D., Pilia M., 2021, [MNRAS](#), **507**, L1

Manchester R. N., Mar D. P., Lyne A. G., Kaspi V. M., Johnston S., 1993, [ApJ](#), **403**, L29

Manchester R. N., Hobbs G. B., Teoh A., Hobbs M., 2005, [AJ](#), **129**, 1993

Marshall F. E., Gotthelf E. V., Zhang W., Middleditch J., Wang Q. D., 1998, [ApJ](#), **499**, L179

Marshall F. E., Gotthelf E. V., Middleditch J., Wang Q. D., Zhang W., 2004, [ApJ](#), **603**, 682

Marshall F. E., Guillemot L., Harding A. K., Martin P., Smith D. A., 2015, [ApJ](#), **807**, L27

Mereghetti S., Rigoselli M., Taverna R., Baldeschi L., Crestan S., Turolla R., Zane S., 2021, [ApJ](#), **922**, 253

Middleditch J., Pennypacker C., 1985, [Nature](#), **313**, 659

Middleditch J., Marshall F. E., Wang Q. D., Gotthelf E. V., Zhang W., 2006, [ApJ](#), **652**, 1531

Mignani R. P., Sartori A., de Luca A., Rudak B., Słowińska A., Kanbach G., Caraveo P. A., 2010, [A&A](#), **515**, A110

Mignani R. P., et al., 2019, [ApJ](#), **871**, 246

Owen R. A., et al., 2011, [A&A](#), **530**, A132

Pietrzyński G., et al., 2019, [Nature](#), **567**, 200

Ransom S. M., Eikenberry S. S., Middleditch J., 2002, [AJ](#), **124**, 1788

Ray P. S., et al., 2011, [ApJS](#), **194**, 17

Reynolds C. S., et al., 2024, in den Herder J.-W. A., Nikzad S., Nakazawa K., eds, Society of Photo-Optical Instrumentation Engineers (SPIE) Conference Series Vol. 13093, Space Telescopes and Instrumentation 2024: Ultraviolet to Gamma Ray. p. 1309328, doi:10.1117/12.3022993

Rigoselli M., Mereghetti S., Halpern J. P., Gotthelf E. V., Bassa C. G., 2024, [ApJ](#), **976**, 228

Riles K., 2023, [Living Reviews in Relativity](#), **26**, 3

Seward F. D., Harnden Jr. F. R., Helfand D. J., 1984, *ApJ*, **287**, L19
 Takata J., Wang H. H., Lin L. C. C., Kisaka S., 2024, *ApJ*, **965**, 126
 Torii K., Tsunemi H., Dotani T., Mitsuda K., 1997, *ApJ*, **489**, L145
 Torii K., Tsunemi H., Dotani T., Mitsuda K., Kawai N., Kinugasa K., Saito
 Y., Shibata S., 1999, *ApJ*, **523**, L69
 Townsley L. K., Broos P. S., Feigelson E. D., Garmire G. P., Getman K. V.,
 2006, *AJ*, **131**, 2164
 Tuo Y., Serim M. M., Antonelli M., Ducci L., Vahdat A., Ge M., Santangelo
 A., Xie F., 2024, *ApJ*, **967**, L13
 Verner D. A., Ferland G. J., Korista K. T., Yakovlev D. G., 1996, *ApJ*, **465**, 487
 Wang Q. D., Gotthelf E. V., 1998, *ApJ*, **494**, 623
 Wette K., 2023, *Astroparticle Physics*, **153**, 102880
 Wilms J., Allen A., McCray R., 2000, *ApJ*, **542**, 914
 Xie F., et al., 2024, *ApJ*, **962**, 92
 Zane S., et al., 2011, *MNRAS*, **410**, 2428
 Zheng J.-T., Ge M.-Y., Li X.-H., 2023,
 Research in Astronomy and Astrophysics, **23**, 115007
 Zubia E., Espinoza C. M., Antonopoulou D., Ho W. C. G., Kuiper L., García
 F., del Palacio S., 2026, *A&A*, in press

This paper has been typeset from a $\text{\TeX}/\text{\LaTeX}$ file prepared by the author.